Chapter 8

MAGNETOSPHERIC AND HIGH LATITUDE IONOSPHERIC ELECTRODYNAMICS

W.J. Burke, D.A. Hardy, and R.P. Vancour

This chapter deals with the volume of space that is bounded externally by the magnetopause and internally by the plasmapause and the high latitude ionosphere at an altitude of 300 km. The magnetopause separates regions of space dominated by the earth's magnetic field (magnetosphere) and by the shocked solar wind (magnetosheath). Earthward of the plasmapause, dynamics are generally controlled by corotation rather than by solar wind driven convection. The arbitrarily chosen, low altitude boundary in the ionosphere represents a transition below which the effects of the earth's neutral atmosphere are dominant. From the viewpoints of both cause and effect, the chapter is something less than self contained. Without the geomagnetic field (Chapter 4) and the solar wind (Chapter 3), there would be no magnetosphere and no magnetospheric electrodynamics; without solar irradiance (Chapter 2), there would be much less of an ionosphere. Without magnetospheric electrodynamics, there would be no aurora (Chapter 12), no high-latitude currents (Chapter 4), no radiation belts (Chapter 5), and no problems with spacecraft charging (Chapter 7).

The term "electrodynamics" encompasses a complex of processes by which charged particles move about in the magnetosphere-ionosphere system. The nature of the processes varies from region to region within the system. Magnetic merging at the magnetopause and field-aligned potential drops above the auroral ionosphere are examples of localized, electrodynamic processes. They are unified as electrodynamic processes in that they emerge, with appropriate boundary conditions, as solutions of the Vlasov-Maxwell equations. General solutions of the Vlasov-Maxwell equations over the entire magnetosphere-ionosphere system are well beyond present capabilities. Some success, however, has been achieved by considering elements of the system in relative isolation. This provides insight into how system elements evolve in response to external inputs. Since the entire system is electrically coupled, the isolated element approach is self-limiting. As one element evolves it affects processes in other elements of the system. The main goals of this chapter are to describe the various system elements and indicate, in a qualitative sense, how they are electrically coupled.

In dealing with the earth's magnetosphere three things quickly impress the mind. First, there is almost nothing there. Particle densities in the plasma sheet range up to about $1/cm^3$. With present technology, laboratory vacuum systems are able to get down to densities of $10^{10}/cm^3$. Second, the volume of space occupied by the magnetosphere is considerable. Typical magnetospheric dimensions are of the order of 10 R_E (1 R_E = 6.4 × 10^3 km). Third, when concentrated to global scales the effects of magnetospheric processes are impressive. The third point which is illustrated in Figure 8-1 provides a convenient point of departure for this survey of magnetospheric and high-latitude ionospheric processes. The figure exemplifies the spatial distribution of visible radiation observed by means of an optical imaging system on a Defense Meteorological Satellite Program (DMSP) satellite. City lights provide an easily recognized map of the western half of North America. The total energy emitted by auroral forms over the northern tier of Canadian provinces rivals or exceeds the combined ground emissions from the United States and Canada. Auroral emissions are largely due to plasma sheet electrons with energies of a few keV impacting the E layer of the ionosphere. The instantaneous locus of plasma sheet electron precipitation is called the auroral oval. Global imagery from satellites such as DMSP have shown that the auroral oval may be approximated by circular bands surrounding the geomagnetic poles. The centers of the circles are offset by ~3° to the night sides of the magnetic poles. The radii of the circle, the widths of the bands and the intensity of emissions vary with the level of geomagnetic activity. However, at all times the auroral oval exists and acts as a major sink for magnetospheric particles and energy. The particles and energy lost by the magnetosphere due to auroral precipitation ultimately come from the solar wind. Thus, an estimate of global precipitation loss is also an estimate of the efficiency of solar wind/magnetospheric interactions required to maintain the auroras.

During periods of moderate geomagnetic activity the auroral oval can be approximated as a circular band extending from 75° to 65° magnetic latitude. The area of such a band is $10^{17}cm^2$. The mean flux of electrons into the

CHAPTER 8

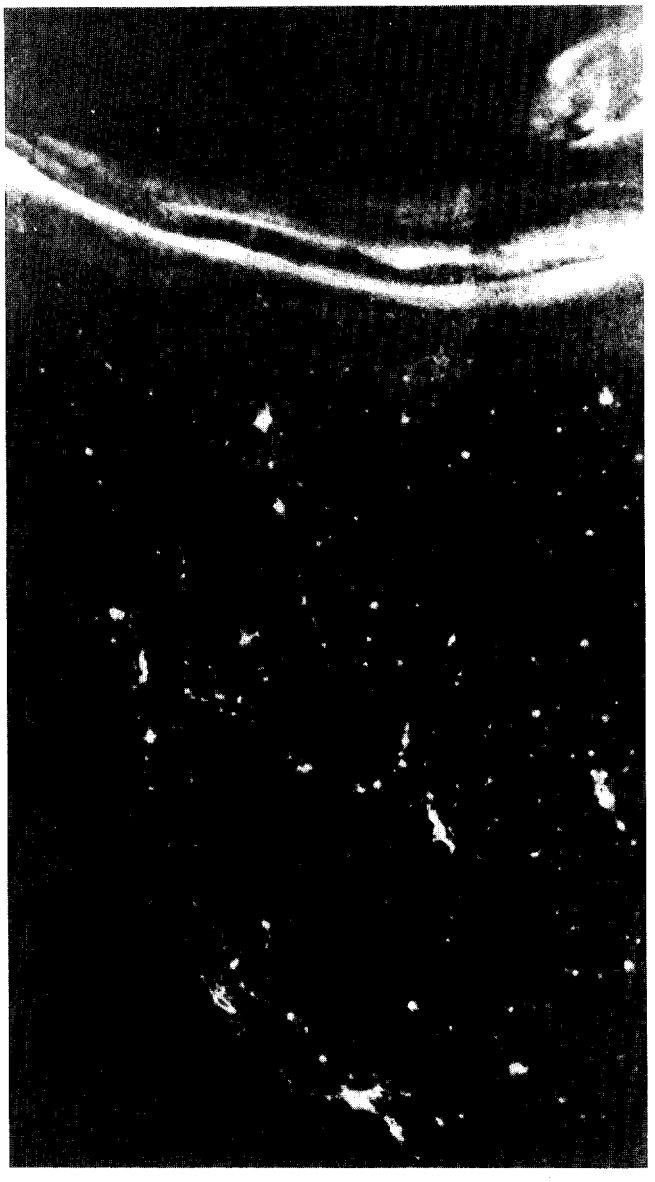

Figure 8-1. DMPS imagery from over western North America.

auroral oval is $\sim 10^9$ cm^{-2}s^{-1}. Thus under steady state conditions the solar wind must supply electrons to the magnetosphere at a rate of 10^{26}/s. The average energy of precipitating electrons is of the order of 1 keV. The energy loss due to electron precipitation alone is $\sim 10^{10}$ W. Similar or larger amounts of solar wind energy must be supplied to account for ionospheric Joule heating and for maintaining the ring current. The central focus of this chapter is to outline the present understanding of how 10^{26} electrons per second and tens of billions of watts are extracted from the solar wind to drive magnetospheric and ionospheric electrodynamic processes.

8.1 MAGNETOSPHERIC BOUNDARY INTERACTIONS

In describing interactions between the solar wind and the earth's magnetosphere two coordinate systems are usefully employed: geocentric solar-ecliptic (GSE) and solar magnetospheric (GSM) coordinates. Both coordinate systems, which are described in detail in Chapter 4, have their origins at the center of the earth with the X axes positive toward the center of the sun; that is, $X_{sc} = X_{sm}$. The Z_{se} axis is normal to the ecliptic plane and positive toward the north. The Y_{se} that completes the right hand system is positive toward local dusk. The Z_{sm} axis is coplanar with the earth's magnetic moment vector (**M**) and the X_{sm} axis. It is positive toward ecliptic north. The Y_{sm} axis, which always lies in the SM equatorial plane, completes the right hand coordinate system. For a radially flowing solar wind ($\mathbf{V}_s = -V_s\hat{X}_{se} = -V_s\hat{X}_{sm}$, where $\hat{X}_{se}$ and $\hat{X}_{sm}$ are unit vectors along X_{se} and X_{sm}, respectively) the angle between **M** and Z_{sm} gives the magnetic latitude of the magnetospheric subsolar point. Note that due to 11° offset between **M** and the earths rotational axis and to the 23.5° angle between the equatorial and ecliptic planes the magnetic latitude of the subsolar point is subject to $\pm 34.5°$ combined seasonal and diurnal variations. The GSM is superior to the GSE system for ordering data relevant to interactions between the solar wind and the magnetosphere.

8.1.1 The Magnetopause

The shape of the "steady state" magnetosphere is determined from the force balance equation

$$\nabla \cdot [\underline{\underline{P}} + \underline{\underline{T}}] = 0 \qquad (8.1)$$

where $\underline{\underline{P}}$ and $\underline{\underline{T}}$ are the total pressure and the Maxwell stress tensors, respectively. The total pressure tensor is made up of two parts due to the dynamic and thermal pressures of the solar wind components:

$$\underline{\underline{P}} = 2n_s m_p \mathbf{V}_s \mathbf{V}_s + p_{si} + p_{se} \qquad (8.1)$$

where n_s is the solar wind density, m_p the mass of a proton; p_{si} and p_{se} are the thermal pressures of solar wind ions and electrons, respectively. The factor of 2 accounts for specular reflection of incoming particles. The shape of the magnetopause on the dayside can be calculated by numerical means using a simplified force balance

$$2n_s m_p V_s^2 (-\hat{X}_{se} \cdot \hat{n}_M)^2 = \frac{B_T^2}{2\,\mu_o}, \qquad (8.3)$$

where μ_o is the permitivity of free space, $\hat{n}_M$ is an outward directed unit vector normal to the magnetopause, and $\mathbf{B}_T$

the total magnetic field at the magnetopause. $\mathbf{B}_T$ is a superposition of fields due to the earth's dipole $\mathbf{B}_D$, to the currents flowing on the magnetopause $\mathbf{B}_M$, and to other currents distributed in the magnetosphere. Beyond the magnetopause $\mathbf{B}_M$ exactly cancels the internal fields. To a very good approximation at the subsolar point of the magnetopause

$$|\mathbf{B}_T| = 2|\hat{n}_M \times \mathbf{B}_D|. \tag{8.4}$$

In the magnetic equatorial plane

$$\mathbf{B}_D = \frac{B_o}{L^3}, \tag{8.5}$$

where $B_o = 3 \times 10^4$ nT is the strength of the earth's field at the surface on the magnetic equator and L is the distance from the center of the earth in earth radii (R_E). Substitution of Equations (8.4) and (8.5) into (8.3) gives the distance to the magnetopause near the subsolar point

$$L_M = \left(\frac{B_o^2}{\mu_o n_s m_p V_S^2}\right)^{1/6}. \tag{8.6}$$

For a solar wind density and velocity of 5/cm^3 and 400 km/s, $L_M = 9$. The shape of the dayside magnetopause was calculated by Mead and Beard [1964] and by Olson [1969] using iterative numerical techniques in which the tilt of the dipole was ignored and included, respectively. Figure 8-2 shows a meridional cross section of the magnetosphere calculated with $L_M = 10$ in the Mead and Beard model. The locus of dipole field lines (dashed lines) in comparison with the calculated total field strikingly illustrates the effects of the solar wind on the overall magnetic topology. Magnetic field lines on the dayside are compressed while those on the nightside are elongated. Note that in this model, field lines intersecting the earth at magnetic latitudes greater than 83° are swept back to the nightside by the solar wind. There are a pair of singular points on the magnetopause at separatrices between field lines closing on the day and night sides. These points correspond to the dayside cusps.

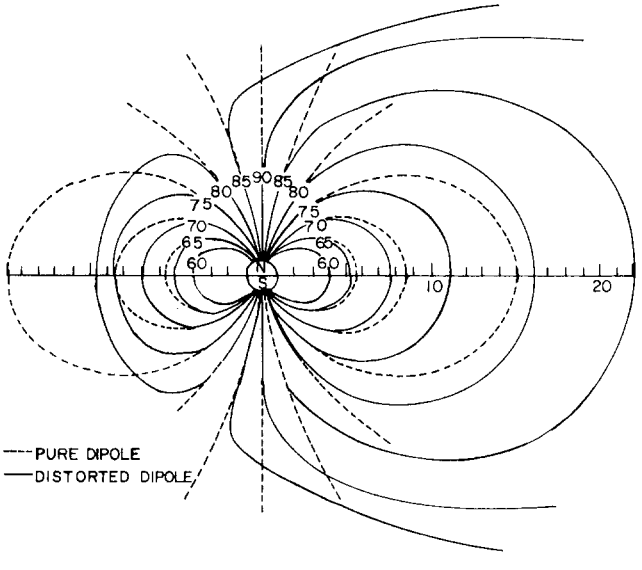

Figure 8-2. Model of earth's magnetic field distorted by the solar wind [Mead and Beard, 1964].

The models just discussed do not describe the nightside of the magnetotail adequately. One reason is apparent from a consideration of Equation (8.2). On the dayside of the magnetosphere, the dynamic pressure of the solar wind dominates over the thermal pressures. On the nightside, with plasma flow almost tangential to the magnetopause ($\mathbf{V}_s \cdot \hat{n}_M \approx 0$), the converse is true. An early model [Johnson, 1950] of the magnetosphere had a tear drop shape with the closing distance determined by the solar wind Mach number. Piddington [1963] suggested that, in flowing past the magnetosphere, the solar wind exerts tangential stresses at the boundary. Such stresses draw the nightside of the magnetosphere into an elongated magnetotail. In the absence of significant plasma within the magnetotail, the tangential force exerted by the solar wind on the magnetosphere is

$$F_T = \frac{B_{MT}^2}{2\mu_o} \pi R_{MT}^2 \tag{8.7}$$

where B_{MT} and R_{MT} are the field strength and radius of the magnetotail, respectively. There are, however, distributed currents in the inner magnetosphere (the ring current) and in the magnetotail (the neutral sheet) currents, whose effects must be included in realistic stress calculations.

8.1.2 Convection

In many cases, the magnetosphere-solar wind interaction is well described by steady state equations such as Equation (8.1). The equilibrium represented by these equations is, however, dynamic rather than static. Only a dynamic situation is consistent with existing high latitude current systems. These currents result from ionospheric convection which is driven by magnetospheric convection [Gold, 1959]. Magnetospheric convection is in turn driven by the solar wind. That is, energy is extracted from the solar wind by the magnetosphere, and at least some of that energy is dissipated in the ionosphere. Two mechanisms for transferring energy to the magnetosphere have been developed over the last two decades: viscous interactions [Axford and Hines, 1961] and magnetic merging [Dungey, 1961]. Both models explain many qualitative features of magnetospheric convection and auroral particle energization. Recent satellite observations suggest that both mechanisms are operative,

but in more complex ways than envisaged by early proponents.

The Axford-Hines model postulates that the magnetosheath plasma exerts a viscous force on a layer of unspecified thickness inside the magnetopause. Magnetic field lines threading this layer are dragged in the antisolar direction and are stretched to great distances in the magnetotail. As elongated flux tubes move out of the viscous interaction layer they snap back to a more dipolar configuration. In the rest frame of the earth this motion of magnetic field lines appears as an electric field, $\mathbf{E} = -\mathbf{V} \times \mathbf{B}$. A magnetospheric equatorial projection of the convection pattern generated in the viscous interaction model is given in Figure 8-3. When mapped to ionospheric altitudes, assuming that

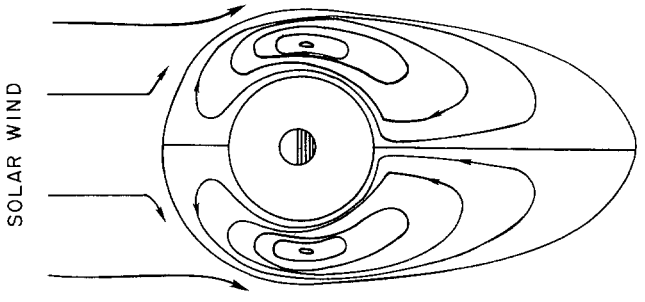

Figure 8-3. Equatorial projection of convection pattern in viscous interaction model.

$\mathbf{E} \cdot \mathbf{B} \approx 0$, the model reproduces the general features of the polar/auroral current system (Chapter 4). Note that plasma trapped on elongated flux tubes is adiabatically heated as the flux tubes convect earthward and shrink in volume.

The second model postulates that the dynamic interaction between the solar wind and the magnetosphere proceeds by means of a magnetic merging process. The simplest features of this phenomenon are illustrated in Figure 8-4.

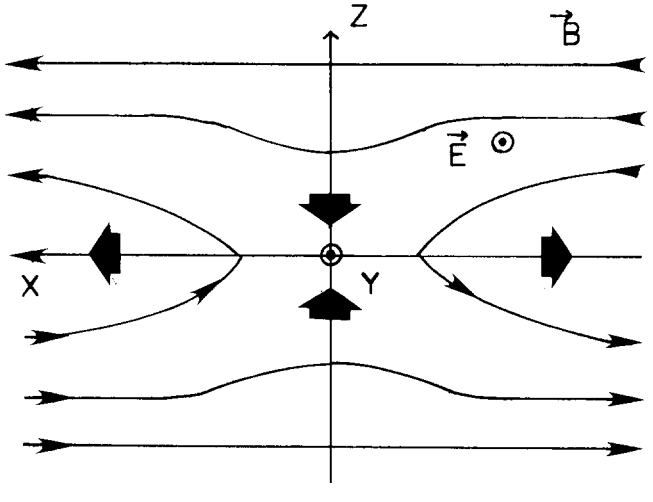

Figure 8-4. Magnetic field geometry and electric field required for magnetic merging.

Consider a magnetic field that at great distances above (below) the X-Y plane points in the + (−) X direction. In the presence of an electric field E_Y, magnetic field lines convect toward the X-Y plane. At the neutral line (X = 0, Z = 0), magnetic field lines from the upper half space merge with field lines of the opposite polarity from the lower half space. To the left (right) of the neutral line, merged magnetic field lines cross the X-Y plane with a + (−) Z component, and $\mathbf{E} \times \mathbf{B}$ convect away from the neutral line in the + (−) direction. Two necessary conditions for magnetic merging are magnetic field of opposite polarity across some plane and an electric field component that is tangent to the plane.

Before considering how magnetic merging might apply to the magnetosphere, it is useful to distinguish between several possible magnetic topologies. It is well known that a weak interplanetary magnetic field (IMF) is carried by the solar wind. Except for a small correction term in the force balance equation, the IMF plays no obvious role in the viscous interaction model. The magnetic merging model assigns important roles to the IMF because this model requires three types of magnetic field lines: (1) IMF lines with both "feet" in the interplanetary medium, (2) closed field lines with both "feet" in the earth, and (3) open field lines with one "foot" on earth and the other in the solar wind. Dungey [1961] pointed out that when the IMF has a southward component, magnetic merging can occur near the subsolar point of the magnetopause. The idea is illustrated in Figure 8-5 which can be viewed either as a snap shot or as

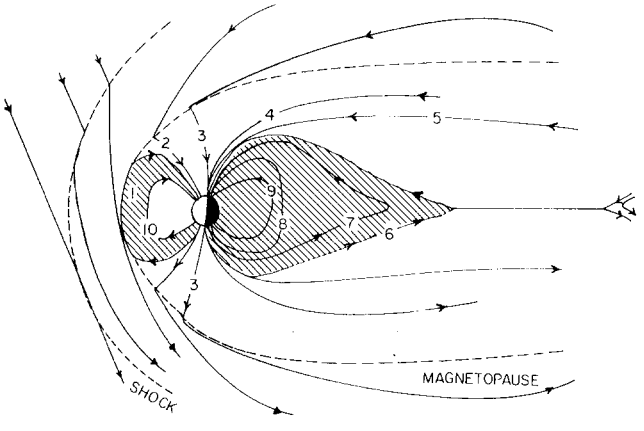

Figure 8-5. Snapshot of magnetic merging between southward IMF and the earth's magnetosphere.

a time history of an individual field line. As southward directed IMF lines are convected up against compressed dipolar field lines, merging occurs at time ①. Because one foot of a newly merged field line is imbedded in the solar wind, the whole field line is dragged in the antisolar ($-X_{sm}$) direction. In an earth-stationary frame of reference the motion of the ionospheric foot of the field line appears to result from a dawn to dusk electric field. Times ② through ⑤ show the various stages of antisunward motion of an open

field line. At time ⑥, a portion of the field line has convected to the magnetic equatorial plane where it reconnects with an open field line from the conjugate ionosphere. Under the influence of the dawn to dusk electric field, the field line then convects earthward (times ⑦ through ⑨). Eventually, reconnected field lines move to the dayside (time ⑩) where they are in position to continue the merging-reconnection cycle.

The magnetospheric convection patterns predicted by the viscous interaction and magnetic merging models with a southward IMF are quite similar. Empirical evidence from near the magnetopause indicates that both viscous and magnetic merging processes occur [Eastman et al., 1976; Russell and Elphic, 1979; Mozer et al., 1979]. That many observational studies have shown high correlations between southward turnings of the IMF and the onset of magnetic activity indicates a dominant role for energy transfer by a merging process. As discussed in Section 8.5.1, this surmise is supported by modifications observed in polar cap (open field line) convection patterns with variations in the Y_{SM} component of the IMF and when the Z_{SM} component is northward. Finally, we mention that currently merging is thought to occur sporadically rather than as a steady state process [Haerendel et al., 1978], and in the vicinity of the dayside cusps rather than near the subsolar point [Crooker, 1977; Crooker, 1979].

8.1.3 Boundary Layers

Before considering the dynamics of the closed portion of the magnetosphere, let us return briefly to our original question of how 10^{26} particles/s gain entry to the plasma sheet. Between 10^{28} and 10^{29} solar wind particles/s impact the dayside magnetopause. Thus, an entry efficiency of less than 1% is sufficient to maintain the plasma sheet. Our understanding of how magnetosheath plasma gains entry to the magnetosphere and influences its interior dynamics has been evolving rapidly over the last decade. Under such circumstances, it is not unusual to encounter a multiplicity of nomenclatures that will probably be simplified as relationships between various boundary plasma regimes become more evident. Vasyliunas [1979] has defined magnetospheric boundary layers as regions of space threaded by magnetic field lines of the magnetosphere but populated by plasma similar to that found in the magnetosheath. The four regions satisfying this definition are (1) the plasma mantle, (2) the interior cusp, (3) the low latitude boundary layer (LLBL), and (4) the plasma sheet boundary layer. Figure 8-6a is a schematic representation of the magnetospheric loci of these regimes. Somewhat speculative representations of their ionospheric projections and their "source-relationships" to the plasma sheet are given in Figures 8-6b and 8-7, respectively. The plasma mantle is found on open magnetic field lines; the remaining three regions are found in closed field line portions of the magnetosphere.

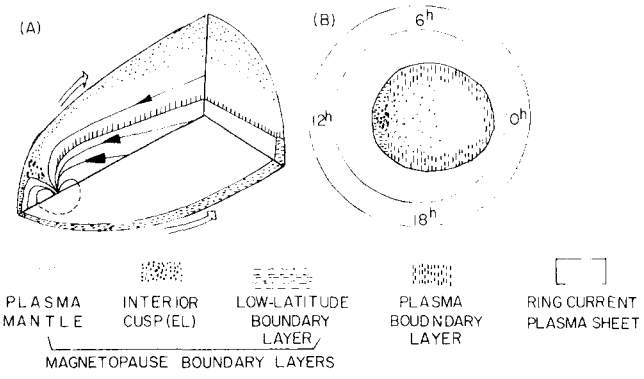

Figure 8-6. (a) Schematic diagram of various observed magnetospheric boundary layers; (b) their mapping down to the ionosphere along magnetic field lines [Vasyliunas, 1979].

The plasma mantle was first identified as a magnetosheath-like plasma flowing along magnetic field lines inside the magnetopause in the near-earth lobes of the magnetotail [Rosenbauer et al., 1975]. The plasma density and the spatial thickness of the mantle are greatest during periods of southward IMF [Sckopke et al., 1976]. The mantle is also observed in the lobes of the magnetotail at lunar distance ($X_{SM} = -60\ R_E$) near the ecliptic plane [Hardy et al., 1975]. Mantle particles are believed to enter the magnetosphere near the dayside cusp. Dawn to dusk electric fields cause particles to convect in the antisunward direction so that particles that mirror at low altitudes find themselves on open field lines as they rise from their mirror points. The same dawn to dusk electric field causes the mantle particles to drift toward the equatorial plane as they move away from the earth. Pilipp and Morfill [1978] suggested that mantle particles may be one source of plasma sheet particles.

As the name suggests, the "interior cusp" refers to the region of closed magnetic field lines passing through or just equatorward of the cusp. Magnetosheath plasma diffuses into this region. As opposed to the mantle or the LLBL, the plasma of this region, which is also called the entry layer, is relatively stagnant. However, depending on the strength and direction of convective electric fields in the cusp, it is possible to think of the interior cusp plasma as a partial source of both the mantle and the LLBL.

Along the dawn and dusk meridians near the magne-

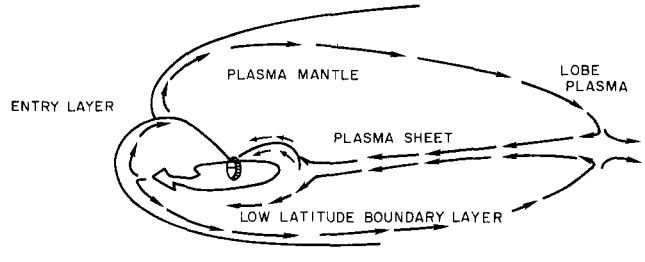

Figure 8-7. A model of magnetospheric circulation for filling the plasma sheet [Freeman, 1979].

tospheric equatorial plane, the LLBL is characterized by magnetosheath-like plasma flowing in the antisunward direction. The thickness of this layer ranges up to ~1 R_E. As shown in Figure 8-6a, the LLBL has been observed to great distances in the antisolar direction. The density of plasma within the layer is about a factor of four less than that of the adjacent magnetosheath [Sckopke et al., 1981]. Electrons within the layer have trapped pitch angle distributions [Eastman and Hones Jr., 1979]. Whether the LLBL is maintained through a diffusive and/or an impulsive [Lemaire and Roth, 1978] entry process is currently a matter of debate. Sckopke et al. [1981] estimate that a diffusion coefficient of $10^9 m^2/s$ is required to maintain the observed LLBL. Figure 8-6a shows the plasma boundary layer together with the LLBL as forming a continuous envelope surrounding the hot plasma contained in the central plasma sheet. The physical processes which connect the LLBL and/or the mantle with the plasma boundary layer and with the central plasma sheet are not known at this time. It is currently believed that discrete arcs in the auroral oval map to the boundary rather than to the central plasma sheet. Within the plasma sheet boundary, rapidly flowing plasmas are observed. These flowing plasmas come from spatially limited acceleration regions called "magnetospheric fireballs" [Frank et al., 1976]. Whether the energization process in fireballs results from magnetic reconnection or some other process is still another open question.

8.2 THE PLASMA SHEET

The earth's plasma sheet is the highly dynamical region of the earth's magnetosphere that acts as a depository for auroral particles. It is a region of closed magnetic field lines. Before being first detected by the Soviet satellites Luna I and Luna 2 [Gringanz et al., 1961], somewhat strangely, this important region of the magnetosphere was not anticipated theoretically. Equatorial and noon-midnight meridional projections of the plasma sheet are given in Figures 8-8 and 8-9, respectively [Vasyliunas, 1972]. Both projections show that the plasma sheet extends for great distances in the $-X_{SM}$ direction. The plasma sheet has a distinct inner edge that varies as a function of local time and the level of geomagnetic activity [Vasyliunas, 1968; Frank, 1971]. The dynamics of the inner edge of the plasma sheet are well understood theoretically and are discussed in Section 8.6.2. The equatorial thickness of this boundary is ~1 R_E and is marked by a cooling of electron temperatures. Just tailward of this boundary plasma sheet electrons have an average energy of ~1 keV. During periods of substorm injections, the temperature of electrons may rise to ~10 keV. Temperatures of plasma sheet ions tend to be higher than those of electrons by a factor of 2 or more.

Figure 8-10 is a cross sectional view of the magnetotail portion of the plasma sheet. It has a minimum thickness in the mid-tail region and flares to a maximum thickness near

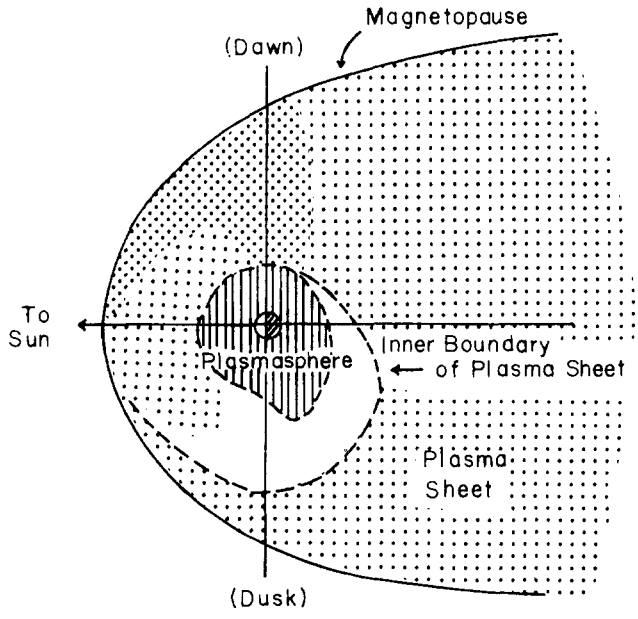

Figure 8-8. The distribution of plasma sheet electrons in the equatorial plane [Vasyliunas, 1972].

the dawn and dusk flanks of the tail. At lunar distance ($X_{SM} = -60\ R_E$) the tail radius is ~25 R_E. The average half-thickness of the mid-tail plasma sheet is ~3 R_E. During the expansion phase of substorms, the thickness of the plasma sheet in the tail decreases and then expands during the recovery phase [Hones et al., 1973]. At lunar distance the average density of the plasma sheet is ~0.1 cm^3. The electron and proton temperatures are ~0.25 and 2.5 keV, respectively [Rich et al., 1973].

The remainder of this subsection is concerned with the physical mechanisms responsible for particle energization and precipitation in the plasma sheet. Energization processes are classified as either adiabatic or non-adiabatic. Examples of non-adiabatic energization are neutral sheet acceleration [Speiser, 1967], stochastic wave-particle acceleration, and heating derived from magnetic field reconnection and annihilation. Although these are undoubtedly important sources of particle energy, we limit ourselves to describing adiabatic energization in some detail. Particle precipitation is main-

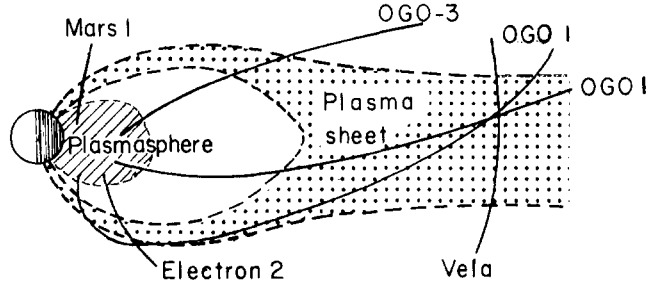

Figure 8-9. The distribution of nightside, plasma sheet electrons in meridional plane [Vasyliunas, 1968].

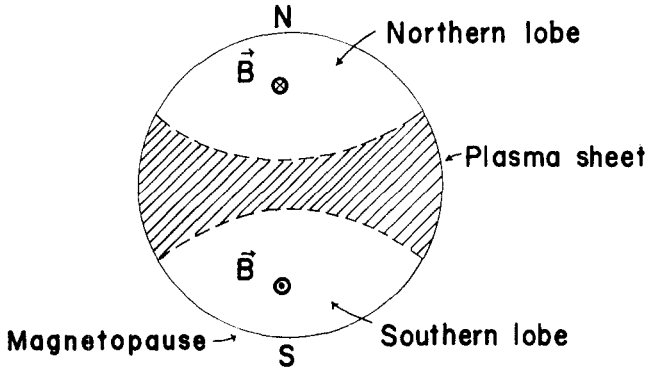

Figure 8-10. Cross-sectional view of magnetotail looking earthward.

tained or enhanced either by magnetic-field aligned electric fields ($E_\parallel$) or by pitch angle diffusion. $E_\parallel$ is very important for discrete auroral arc formation. Pitch angle diffusion results from wave particle interactions. Here we summarize briefly the collective plasma modes responsible for these phenomena.

8.2.1 Adiabatic Motion in the Plasma Sheet

The adiabatic energization of plasma sheet particles involves the related concepts of adiabatic invariance and guiding center motion. The general concept of adiabatic invariance comes from classical Hamilton-Jacobi theory [TerHaar, 1964]. If a system executes a periodic motion in a force field (F) that changes slowly in time with respect to the period (T)

$$\frac{1}{F}\frac{dF}{dt} \ll \frac{1}{T}$$

then the quantity

$$I = \oint p\, d\, q,$$

where p and q are canonical momentum and coordinate variables, is a constant of the motion known as an adiabatic invariant. Charged particles moving in the earth's magnetic field may have as many as three periodicities due to their gyration, bounce, and drift motions. The three adiabatic invariants associated with these periodicities are

(1) the magnetic moment

$$\mu = \frac{mv_\perp^2}{2B}, \tag{8.8}$$

where $v_\perp$ is the component of velocity perpendicular to the magnetic field,

(2) the longitudinal invariant

$$J = \oint p_\parallel\, ds, \tag{8.9}$$

where $p_\parallel$ and ds are momentum component and distance along B, and

(3) the flux invariant

$$\Phi = \oint \mathbf{A} \cdot d\ell \tag{8.10}$$

where $\mathbf{A}$ is the magnetic vector potential and $d\ell$ a distance element along a particle drift trajectory [Northrop, 1963; Rossi and Olbert, 1970]. Most plasma sheet particles either precipitate or follow drift trajectories that intersect the magnetopause before they can drift all the way around the earth. Thus, in the plasma sheet only the first and second invariants are of interest. The third invariant is important for understanding the ring current and radiation belts (Chapter 5).

At this point it is useful to introduce the related concepts of pitch angle and magnetic mirroring. The pitch angle of a particle (α) is defined as the angle between its instantaneous velocity and the magnetic field

$$\alpha = \cos^{-1}\left(\frac{\mathbf{v}\cdot\mathbf{B}}{|\mathbf{v}|\,|\mathbf{B}|}\right).$$

Magnetic mirroring results from the constancy of a particle's magnetic moment and total energy. The total energy of a non-relativistic particle of mass m and charge q moving with a velocity v in combined magnetic and electric fields is

$$\varepsilon = 1/2\, mv_\parallel^2 + \mu B + q\Psi \tag{8.11}$$

where Ψ is the electrical potential. The component of force exerted along $\mathbf{B}$ is

$$m\frac{dv_\parallel}{dt} = -\mu\frac{\partial B}{\partial s} - q\frac{\partial \Psi}{\partial s}. \tag{8.12}$$

The second term on the right hand side of Equation (8.12) is due to field-aligned electric field components that are discussed regarding auroral arc formation. The first term on the right hand side of Equation (8.12) is the magnetic mirror force. A particle at the magnetic equator (s = 0) with pitch angle α_{eq} can move earthward along B until its pitch angle reaches 90° ($v_\parallel = v_{cos}\alpha = 0$). At this point, it is reflected by the mirror force toward the magnetic equator. The strength of the magnetic field at the mirror point is designated B_M. The total kinetic energy of a particle at its mirror point is $1/2mv^2 = \mu B_M$. Since in general $\mu = 1/2mv^2\,(\sin^2\alpha)/B$, the magnetic mirroring condition, in the absence of $E_\parallel$, is often written

$$\sin^2\alpha = \frac{B}{B_M}. \tag{8.13}$$

The line integration for the longitudinal invariant proceeds from the magnetic equator to the mirror distance (s_M).

The notion of guiding center motion is more general than that of adiabatic motion. Under many circumstances charged particle motions are well-approximated superpositions of motions of guiding centers and gyrational motion about the guiding center. For example, in an uniform magnetic field the equation of motion

$$m \frac{dv}{dt} = q (\mathbf{v} \times \mathbf{B}) \tag{8.14}$$

describes a particle that gyrates with a circular frequency $\Omega = qB/m$ about a field line and moves along the field line (its guiding center) with a constant velocity. In the presence of an external force field $\mathbf{F}$ that is perpendicular to $\mathbf{B}$, the equation of motion

$$m \frac{dv}{dt} = q (\mathbf{v} \times \mathbf{B}) + \mathbf{F} \tag{8.15}$$

can be reduced to the form of Equation (8.14) by transforming to a coordinate system moving with a drift velocity

$$\mathbf{V}_D = \frac{\mathbf{F} \times \mathbf{B}}{qB^2}.$$

In this frame of reference the motion of the particle about $\mathbf{B}$ is purely gyrational.

The most important drifts within the magnetosphere are caused by electric fields

$$\mathbf{V}_E = \frac{\mathbf{E} \times \mathbf{B}}{B^2}, \tag{8.16}$$

magnetic field gradients

$$\mathbf{V}_G = \frac{\mu \mathbf{B} \times \nabla \mathbf{B}}{qB^2}, \tag{8.17}$$

and magnetic field line curvature

$$\begin{aligned} \mathbf{V}_C &= \frac{mv_\parallel^2}{R^2} \frac{\mathbf{R} \times \mathbf{B}}{qB^2} \\ &= mv_\parallel^2 \frac{\mathbf{B} \times (\mathbf{B} \cdot \nabla) \mathbf{B}}{qB^4} \end{aligned} \tag{8.18}$$

where $\mathbf{R}$ is the magnetic field line radius-of-curvature vector. Note that $\mathbf{V}_G$ and $\mathbf{V}_C$ depend on both the particle's energy and charge; $\mathbf{V}_E$ depends on neither. Protons (electrons) gradient and curvature drift toward the west (east). In the nearly dipolar part of the inner plasma sheet, $\mathbf{V}_G$ and $\mathbf{V}_C$ are of comparable magnitudes. Due to sharp magnetic field line curvature across the neutral sheet, $\mathbf{V}_C > \mathbf{V}_G$ in the magnetotail.

With the expressions for the adiabatic invariants [Equations (8.8) and (8.9)] and guiding center drifts [Equations (8.16), (8.17), (8.18)], we may understand (1) the adiabatic heating of magnetospheric plasma, (2) the existence of a ring current, and (3) the position of the inner boundary of the plasma sheet.

Both the viscous interaction and the magnetic merging models require that particles in the nightside plasma sheet be "adiabatically" heated as they convect earthward under the influence of a dawn to dusk electric field. In this motion, each particle's magnetic moment $1/2mv_\perp^2/B$ is a constant. Consider a particle mirroring in the equatorial plane, $J = 0$. As it drifts from, say, 30 R_E in the magnetotail where $B \sim 20$ nT to a distance of 6 R_E where $B \sim 140$ nT, its kinetic energy must increase seven fold. Particles with $J \neq 0$ gain kinetic energy, not only from the conservation of μ, but also from the apparent motion of magnetic mirror points (conservation of J). In moving from equatorial crossings of 30 R_E to 6 R_E, particles find themselves on shorter and shorter field lines. Since $\oint p_\parallel ds$ must be a constant, $p_\parallel$ must increase as particles convect earthward.

From the conservation of energy, it is seen that an increase in particle kinetic energy must be due to a decrease in potential energy. The potential energy is electrical; that is,

$$\frac{d}{dt} (1/2\ mv^2) = q \langle \mathbf{V}_D \cdot \mathbf{E} \rangle . \tag{8.19}$$

The brackets in equation (8.19) are used to represent time averaging over a gyroperiod, and $\mathbf{V}_D$ is the total drift velocity. Since $\mathbf{V}_E$ is perpendicular to $\mathbf{E}$, only $\mathbf{V}_G$ and $\mathbf{V}_C$ contribute. Hines [1963] has shown that the energy gained by "adiabatically compressing" a magnetospheric plasma is equivalent to the kinetic energy gained by gradient and curvature drifting in the direction of an electrostatic potential gradient.

Guiding center motion is the simplest basis for understanding the earth's ring current. The existence of a westward current encircling the earth can be inferred directly from decreases in surface values of the horizontal component of the earth's field during the main and recovery phases of magnetic storms (Chapter 4). The general expression for current density is given by a sum over plasma species

$$\mathbf{j} = \sum_\sigma n_\sigma q_\sigma \mathbf{V}_{D\sigma}$$

Assuming, for simplicity, that the ring current is made up of a single ion species (H^+) then the current density is

$$\mathbf{j}_R = nq (\mathbf{V}_{Di} - \mathbf{V}_{De}) \tag{8.20}$$

Since $\mathbf{V}_E$ is independent of charge, only $\mathbf{V}_G$ and $\mathbf{V}_C$ contribute to Equation (8.20). Recall that for protons (electrons), $\mathbf{V}_G$ and $\mathbf{V}_C$ are westwards (eastwards). In an equiv-

alent fluid description, $\mathbf{j}_R$ is driven by magnetospheric pressure gradients. During the main phases of magnetic storms and the expansion phases of substorms, particles are energized and injected into the inner magnetosphere by intense electric fields. With the onset of recovery phases the electric fields decrease in intensity and/or are shielded from the inner magnetosphere. Injected particles find themselves on closed, stably trapped orbits in which they gradient and curvature drift around the earth. During recovery, phase these particles are slowly removed from the ring current by precipitation or by charge exchange with low energy neutrals (Chapter 5).

The position and shape of the inner edge of the plasma sheet is determined by the drift motions of plasma sheet particles. $\mathbf{V}_E$ decomposes into drifts due to "convective" ($\mathbf{V}_{E_C}$) and "corotational" ($\mathbf{V}_{E_\Omega}$) electric fields. In the following discussion, we use the symbols E_C to represent the "convective" electric field imposed by the solar wind on the magnetosphere and E_Ω to represent the corotation electric field. The direction of ($\mathbf{V}_{E_\Omega}$) is eastward for all particles. For simplicity let us consider the drift motions of charged particles having pitch angles in the equatorial plane of 90°. The conservation of energy Equation (8.11) immediately tells us that cold ($\mu \simeq 0$) particles are constrained to $\mathbf{E} \times \mathbf{B}$ drift along equipotentials. Particles with non-zero μ drift along surfaces of constant ($\Psi + \mu B/q$).

In the magnetotail, particles predominately drift earthward under the influence of a dawn to dusk E-field. As they approach the earth, electrons acquire significant eastward drifts due to both $\mathbf{V}_G$ and $\mathbf{V}_{E_\Omega}$. Since both of these drifts are eastward, cold electrons with $\mathbf{V}_G = 0$ drift closer to the earth before their eastward drifts dominate over their earthward drifts. For this reason outbound satellites encounter cold before hot electrons at the plasma sheet's inner edge [Kivelson et al., 1979].

The boundary between cold electrons that drift along equipotentials from the tail and those that corotate on closed trajectories is called the zero-energy Alfvén layer or the inner boundary of the plasma sheet. Under steady convective electric field conditions, cold electrons that drift in from the magnetotail without precipitating eventually cross the dayside magnetopause. Thus, the inner boundary of the plasma sheet is the boundary between closed (corotation dominated) and open (convection dominated) equipotentials.

Before calculating the shape of the last closed equipotential, we note that for protons, $\mathbf{V}_G$ and $\mathbf{V}_{E_\Omega}$ are oppositely directed. This leads to more complex drift paths for protons than electrons. Protons with $\mu \neq 0$ can drift earthward of the zero-energy Alfvén boundary in the evening local time sector. The different drift paths of protons and electrons eventually lead to the build up of polarization electric fields near the inner edge of the plasma sheet. The main effects of the polarization field are to shield $\mathbf{E}_C$ from the inner magnetosphere and to distort its dawn to dusk orientation in the plasma sheet.

As a function of distance R and local time ϕ in the equatorial plane of the magnetosphere, the form of the electric potential is

$$\Psi(R, \phi) = \frac{-\Omega B_o R_E^3}{R} + C R^\gamma \sin \phi \qquad (8.21)$$

where $\Omega = 7.3 \times 10^{-5} s^{-1}$ is the angular spin velocity of the earth, C is a constant to be determined, and γ is a parameter that reflects the level of electrical shielding. The case $\gamma = 1$ corresponds to a uniform, dawn to dusk E_C that completely penetrates the inner magnetosphere. Best empirical values of γ are in the range of 2 to 3 [Ejiri et al., 1978; Gussenhoven et al., 1981]. The value of C is determined by noting that $\mathbf{E}_\Omega$ is directed radially inward and $\mathbf{E}_C$ is mostly the Y_{SM} direction. In the dusk sector $\mathbf{E}_\Omega$ and $\mathbf{E}_C$ are oppositely directed. Depending on the strength of $\mathbf{E}_C$, there is a stagnation point along the 1800 LT ($\phi = 3\pi/2$) axis of symmetry where the two fields exactly cancel,

$$\left.\frac{\partial \Psi\left(R, \frac{3\pi}{2}\right)}{\partial R}\right|_{R = R_S} = 0. \qquad (8.22)$$

Substitution of Equation (8.21) into (8.22) gives

$$C = \frac{\Omega B_o R_E^3}{\gamma R_S^{(\gamma+1)}}. \qquad (8.23)$$

Thus,

$$\Psi(L, \phi) = -\frac{\Omega B_o R_E^2}{L_S}\left[\left(\frac{L_S}{L}\right) - \gamma\left(\frac{L}{L_S}\right)^\gamma \sin \phi\right] \qquad (8.24)$$

where we have made the substitution $L = R/R_E$ and $L_S = R_S/R_E$. The common term $\Omega B_o R_E^2$ is ~90 kV. The potential of the stagnation point is

$$\Psi\left(L_S, \frac{3\pi}{2}\right) = -\frac{90}{L_S}[1 + 1/\gamma] \text{ kV}. \qquad (8.25)$$

Since along the $\phi = 3\pi/2$ line $E_C < (>) E_\Omega$ for $L < (>) L_S$, Equation (8.25) gives the potential of the zero-energy Alfvén boundary. By setting the term in brackets on the right hand side of Equation (8.24) equal to $[1 + 1/\gamma]$, we arrive at the equation for the zero-energy Alfvén boundary in the equatorial plane as a function of distance from the center of the earth (L_A) and local time

$$\left(\frac{L_A}{L_S}\right)^{\gamma+1} \sin \phi + (\gamma + 1)\frac{L_A}{L_S} - \gamma = 0. \qquad (8.26)$$

Southwood and Kaye [1979] have shown that to an excellent approximation

$$L_A \approx L_S/\left(1 + \frac{\sqrt{2S}}{\gamma}\right) \qquad (8.27)$$

where $S = |\cos(\phi - \pi/2)/2|$. The solution is exact when $\gamma = 1$. Figure 8-11 shows that the shape of the last equi-

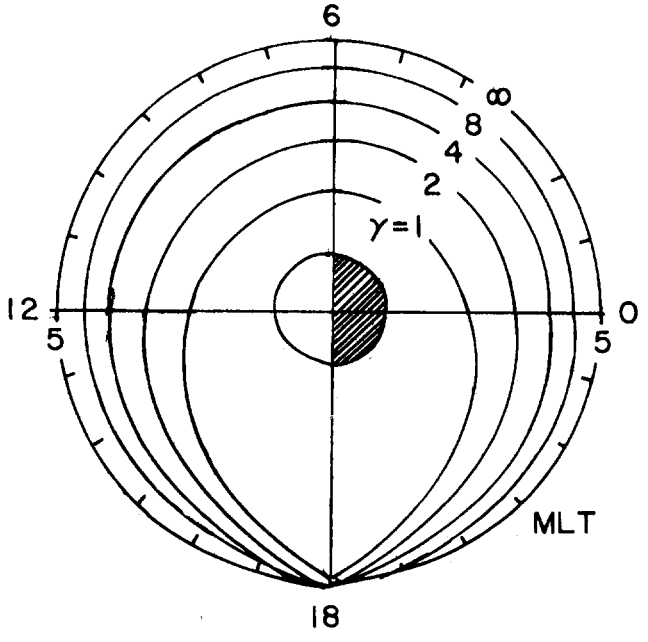

Figure 8-11. Shapes of last closed equipotential for various values of γ [Ejiri et al., 1978].

potential varies from an elongated tear drop for $\gamma = 1$ to a circle for $\gamma = \infty$. Note that Equations (8.26) or (8.27) only allow calculations of the shape, but not the distance to the Alfvén boundary. L_S depends on E_C, which varies with condition in the solar wind and with the level of magnetic activity. It is convenient to defer further comment on the Alfvén boundary until we have discussed its ionospheric projection, the equatorward boundary of diffuse auroral precipitation.

8.2.2 Pitch Angle Diffusion of Plasma Sheet Particles

The final topic to be considered under the heading of general magnetospheric processes is particle precipitation. To anticipate our discussion of the ionosphere, we note that instrumentation on satellites passing through the diffuse auroral ionosphere measure fluxes of electrons and protons that are isotropic over the downcoming hemisphere. The continuous precipitation of plasma sheet electrons and protons into the auroral ionosphere cannot be explained in terms of the individual particle model that we have been using. The problem is illustrated simply in Figure 8-12 where we sketch sequential isocontours of particle distribution functions in the magnetospheric equatorial plane. Figure 8-12a

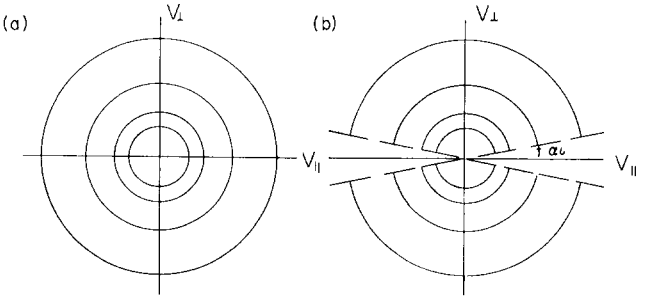

Figure 8-12. Isocontours of distribution functions with (a) isotropic and (b) loss cone distributions.

represents an isotropic population at some initial time. Particles with $\alpha_{eq} \neq 90°$ ($v_\parallel \neq 0$) move along field lines toward their mirror points. If their mirror points are sufficiently deep in the atmosphere, typically altitudes < 200 km, the particles are lost. Otherwise they return to the magnetosphere. If we designate the strength of the magnetic field at an altitude of 200 km as B(200), then Equation (8.13) shows that particles initially with equatorial pitch angles

$$\alpha_{eq} < \alpha_L = \sin^{-1}\left[\frac{B_{eq}}{B(200)}\right]^{1/2} \qquad (8.28)$$

are lost after a few bounce periods. Such particles are said to be in the atmospheric loss cone. For plasma sheet particles α_L is ~2°. Figure 8-12b shows the distribution after several bounce periods as made up of the initial population minus an empty loss cone. Particle motion that conserves μ and J allows no further loss.

Kennell and Petschek [1966] pointed out that above certain particle flux levels, loss cone distribution functions such as shown in Figure 8-12b are unstable to the growth of whistler waves. The waves grow in energy by causing particles to diffuse into the loss cone. To produce strong pitch angle diffusion, that is, maintain isotropy over the loss cone, a resonant condition must be fulfilled. Resonant scattering occurs for particles whose energy is equal to that of the magnetic energy per particle

$$\varepsilon_{Res} \approx \frac{B^2}{2\,\mu_o n}. \qquad (8.29)$$

This model successfully explains flux limits observed for stably trapped ring current particles. The requirement for resonant pitch angle diffusion given in Equation (8.29) was

empirically verified by observations of the proton ring current from Explorer 45 during the magnetic storm of December 1971 [Williams and Lyons, 1974].

An examination of the resonance condition given in Equation (8.29) shows that a whistler mode instability cannot be responsible for strong pitch angle scattering in the plasma sheet. At geostationary altitude (6.7 R_E) in the plasma sheet, B ~ 100 nT and n ~ 1 cm^3. This gives a magnetic field energy density in eV/cm^3 of 2.5 B^2(nT). A resonant energy of ~25 keV is well in excess of mean thermal energies for either electrons or protons in the plasma sheet.

Realizing that whistler mode interactions could not explain the isotropic precipitation of plasma sheet particles, investigators in the 1970s concentrated on sources of electrostatic wave energy. There are two important developments from the decade of which we take note. The first concerns direct observations of broadband electrostatic noise all along magnetic field lines connecting the auroral ionosphere to the equatorial plasma sheet [Gurnett and Frank, 1977]. The amplitudes of observed waves are of sufficient intensity to drive strong pitch angle scattering. The second development concerns the theoretical recognition of the role played by cold plasma for making available free energy contained in anisotropic pitch angle distributions. Cold plasma, of ionospheric origin, in the plasma sheet can produce velocity space gradients in the total distribution functions ($\partial f / \partial v_\perp > 0$) that are unstable to the growth of (N + 1/2) electron cyclotron waves [Young et al., 1973] and lower hybrid ion waves [Ashour-Abdalla and Thorne, 1978]. Numerical studies show that such waves are unstable over restricted ranges of parameter space. Measuring low density, cold plasma embedded in a hot plasma sheet is experimentally difficult. A successful measurement of the cold plasma component is a critical requirement for our understanding plasma sheet processes.

8.3 ELECTRICAL COUPLING OF THE MAGNETOSPHERE AND IONOSPHERE

Before discussing the electrodynamics of the high latitude ionosphere, it is useful to review briefly the theory of magnetosphere-ionosphere coupling. Vasyliunas [1970] has developed a theoretical model that illustrates the physical laws describing how magnetospheric convention couples with the ionosphere. The model is presented in Figure 8-13 in the form of a closed loop of equations (straight lines) and of quantities to be determined (boxes). External sources of particles, cross-magnetospheric potentials, neutral winds in the ionosphere, and so forth, are imposed boundary conditions. Because the loop of equations is self-consistently closed, it can be entered at any point. Let us assume that we have an initial idea about the distribution of magnetospheric electric fields and particles.

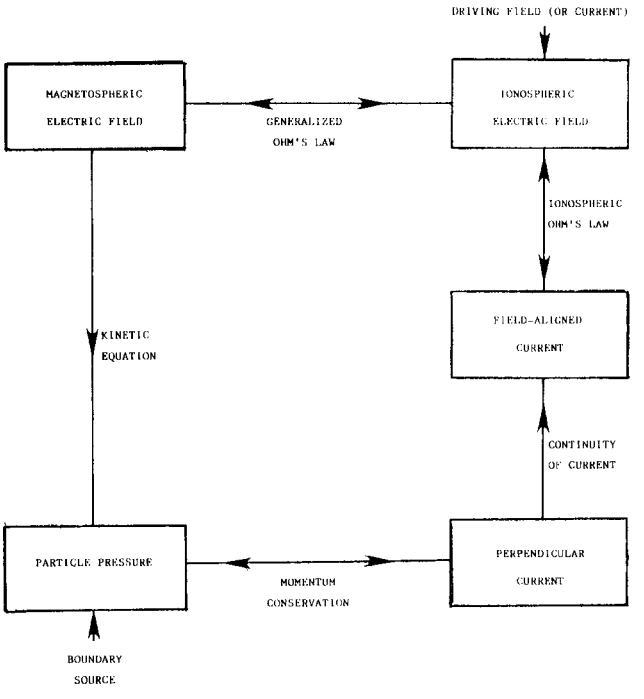

Figure 8-13. Outline of self consistent calculation of magnetospheric convection [Vasyliunas, 1970].

(a) First link: with knowledge of the electric field, we calculate the motion and distribution of protons and electrons in the magnetosphere, and hence the total plasma pressure at any point.

(b) Second link: from the plasma pressure gradients, we calculate the components of the electric current perpendicular to the magnetic field. That is, from the force balance equation

$$\nabla p = \mathbf{j} \times \mathbf{B} \tag{8.30}$$

we calculate

$$j_\perp = \frac{B \times \nabla p}{B^2}. \tag{8.31}$$

For simplicity we have assumed that the pressure is isotropic.

(c) Third link: by calculating the divergence of the perpendicular current and averaging over each flux tube, we obtain ($j_\parallel$) the field-aligned currents (FAC) flowing between the magnetosphere and the ionosphere.

$$\frac{\partial}{\partial s}\left(\frac{j_\parallel}{B}\right) = -\frac{1}{B}\nabla_\perp \cdot \mathbf{j}_\perp \tag{8.32}$$

(d) Fourth link: from the requirement that these field aligned currents be closed by perpendicular Ohmic currents in the ionosphere, we obtain the configuration of the electric

field in the ionosphere. The continuity of ionospheric current requries that

$$\nabla \cdot \mathbf{I} = j_{\parallel} \sin\chi \qquad (8.33)$$

where $\mathbf{I}$ is the height integrated current and χ the inclination of magnetic field lines. In the ionosphere

$$\mathbf{I} = \underline{\Sigma} \cdot (\mathbf{E} + \mathbf{V}_n \times \mathbf{B}) \qquad (8.34)$$

where $\underline{\Sigma}$ is the height integrated conductivity tensor and $\mathbf{V}_n$ is the neutral wind velocity.

(e) Fifth and final link: the ionospheric electric field can be mapped into the magnetosphere, and the requirement that it agree with the magnetospheric electric field assumed at the outset determines the field, and thus closes the system of equations. Except near discrete arcs, the mapping may be done by assuming that magnetic field lines are equipotentials. There is empirical evidence suggesting a functional relationship between $j_{\parallel}$ in discrete arcs and field-aligned potential drops [Lyons et al., 1979]. We note in passing that the Rice University group has successfully simulated the ionospheric features of a magnetospheric substorm using this model [Harel et al., 1981.

From Equations (8.33) and (8.34), it is clear that measurements of $\mathbf{E}$ and $j_{\parallel}$ are critical for understanding the magnetosphere-ionosphere circuit. Measurements of precipitating particle fluxes are needed to (1) understand spatial variation in $\underline{\Sigma}$, (2) identify the dominant carriers of $j_{\parallel}$, (3) calculate field-aligned potential drops, and (4) help distinguish between topologically different regions.

8.4 HIGH LATITUDE ELECTRIC FIELDS

Electric fields at ionospheric altitudes are measured from potential differences between the ends of extended booms on satellites [Fahleson, 1967] and from the $\mathbf{E} \times \mathbf{B}$ drifts of cold plasma [Hanson and Heelis, 1975]. In principle, $j_{\parallel}$ can be determined from particle fluxes. With present technology, full distribution functions of ions and electrons cannot be measured with sufficient accuracy. For this reason, highly sensitive triaxial fluxgate magnetometers [Armstrong and Zmuda, 1973] are used to determine $j_{\parallel}$ from magnetic deflections. Particle fluxes in approximately the energy range 10 eV to 30 keV are measured by means of continuous channel electron multipliers (channeltrons) placed behind electrostatic energy-analyzers [Gold, 1959].

It is useful to explain the format of high latitude data presented in the following subsections by providing an example of the simplest kinds of electric fields and magnetic field deflections expected to be measured by instrumentation on a polar orbiting satellite. Figure 8-14a shows the trajectory of a satellite in circular polar orbit with the ascending node at the dusk (1800 LT) meridian. We define a satellite

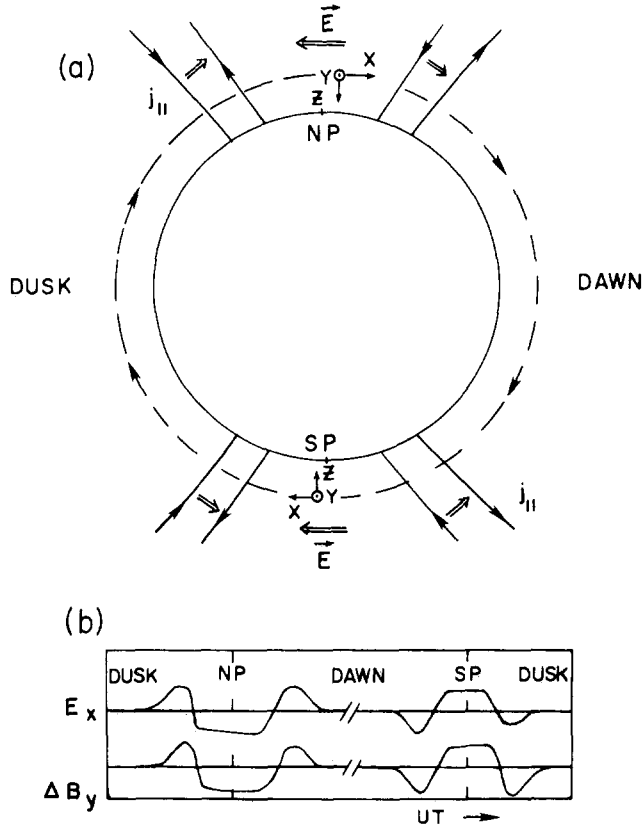

Figure 8-14. (a) Field-aligned currents and electric fields as seen by polar orbitting satellite in dawn-dusk meridian. (b) Idealized electric field and magnetic perturbation measurements.

centered coordinate system; $\hat{X}$ is positive along the satellite velocity; $\hat{Z}$ is positive toward local nadir; $\hat{Y}$ completes the right-hand system. In the dawn-dusk meridian Y is positive in the antisunward direction. At high latitudes in the northern (southern) hemisphere we approximate $\mathbf{B}$ as being along the $+(-)$ Z axis. Figure 8-14a also shows dusk to dawn electric fields in the auroral ovals and uniform dawn to dusk electric fields across the polar caps. The convective electric field reverses directions near the poleward boundary of the auroral oval and goes to zero at the equatorward boundary.

The governing equations are current continuity [Equation (8.33)], Ohm's law [Equation (8.34)] and the Maxwell equation

$$\nabla \times \mathbf{B} = \mu_o \mathbf{j} \qquad (8.35)$$

In the infinite current sheet approximation, these equations may be combined to eliminate $j_{\parallel}$ and reduce to

$$\frac{\partial}{\partial x}[\Delta B_y - \mu_o \Sigma_p E_X] = 0 \qquad (8.36)$$

where ΔB_Y is the deflection of the magnetic field due to $j_{\parallel}$ and Σ_p is the height-integrated Pedersen conductivity

[Smiddy et al., 1980]. Except near local noon at the dayside cusp and near local midnight at the Harang discontinuity where there are significant divergences of the ionospheric Hall current [Rostoker, 1980], Equation (8.36) is a very useful approximation. It tells us that for a uniformly conducting ionosphere, fluctuations in the transverse magnetic field component should track variations in the meridional component of the electric field. Deviations from correlated variations are due to the presence of conductivity gradients. Figure 8-14b is a plot of E_X and ΔB_Y expected over a full orbit assuming a uniform ionospheric conductivity. Positive (negative) slopes in ΔB_Y correspond to regions of current into (out of) the ionosphere. Thus, due to the divergence of ionospheric Pedersen currents, a field-aligned current (FAC) should flow into the ionosphere at the equatorward boundary of the dusk side oval and out at the poleward boundary. The morning side oval currents have the opposite polarity. If there are significant Pedersen currents across the polar cap, the poleward FAC system should be of greater intensity than the equatorward system.

In the following subsections, ΔB_Y is given as a function of time rather than distance. Since satellites at ionospheric altitudes travel at speeds of ~7 km/s, Equation (8.35) can be transformed to give a convenient expression for $j_\parallel$

$$j\left(\frac{\mu A}{m^2}\right) = 0.113\,\frac{\partial\,\Delta B_y(nT)}{\partial\,t(s)}. \qquad (8.37)$$

A current of 1 $\mu A/m^2$ corresponds to a locally unbalanced flux of $\sim 10^9/cm^{-2}s^{-1}$.

Finally, in both the polar cap and the auroral oval we refer to small- and large-scale structures. Small-scale structures have latitudinal dimensions of a few tens of km or less. They are traversed by satellites in a few seconds. Discrete arcs and inverted-V's are examples of small-scale structures. Somewhat arbitrarily, we define large-scale systems as having latitudinal dimensions greater than 100 km. The E field and FAC systems shown in Figure 8-14b are of large scale.

8.5 POLAR CAP ELECTRODYNAMICS

This section treats three topics: (1) large-scale electric field patterns, (2) electron precipitation morphologies, and (3) characteristics of discrete, sun-aligned arcs in the polar cap. Here we use the term "polar cap" to designate the portion of the high latitude ionosphere containing only open magnetic field lines. Precipitating particles on these field lines should be of direct magnetosheath origin. Except possibly during periods of northward interplanetary magnetic field (IMF), cold ionospheric plasma should convect in the antisunward direction under the influence of a dawn to dusk electric field.

8.5.1 Large Scale Electric Fields Patterns

Table 8-1 lists the six polar orbiting satellites launched to date that were capable of measuring ionospoheric electric fields. Data from the double-probe experiment on Injun 5 confirmed the existence of convective reversals near the poleward boundaries of the auroral oval. An inclination of 68° allowed the Atmospheric Explorer (AE-C) driftmeter to measure convective drifts in the oval but usually not in the polar cap. The AE-D satellite had an inclination of 90° but failed ~ 4 months after launch. The orbit was initially close to the noon-midnight meridian and precessed toward dawn-dusk. Because of the high altitude of S3-3, its near-apogee data have been most useful for identifying the small-scale features of auroral arc/inverted-V phenomena. The OGO 6 and S3-2 satellites spent sufficient periods of time near the dawn-dusk meridian to identify the main large-scale features of polar cap convection.

Table 8-1. Satellites capable of measuring electric fields.

SATELLITE	LAUNCH DATE	INCLINATION	INITIAL APOGEE (km)	TYPE INSTRUMENT
Injun 5	Aug 1968	81°	2550	double probe
OGO 6	June 1969	82°	1600	double probe
AE-C	Dec 1973	68°	4000	drift meter
AE-D	Oct 1975	90°	4000	drift meter
S3-2	Dec 1975	96°	1550	double probe
S3-3	Aug 1976	98°	8050	double probe

Two examples of E_X measured by OGO 6 at northern (summer) high latitudes are given in Figure 8-15. Except for small-scale variations, the main features of the expected E_X patterns are found in the auroral oval. The example in the top trace is consistent with a uniform dawn to dusk electric field across the polar cap. In the bottom trace E_X has relatively high (low) values near the morning (evening) flank of the polar cap.

A simplified summary of large-scale electric field patterns identified by Heppner [1972] is given in Figure 8-16.

Type A: Uniform E_X across polar cap. These were observed by OGO 6 only in the northern (summer) polar cap.

Type B: Strong E_X near the morning (evening) flank of the northern (southern) polar cap.

Type D: Strong E_X near the evening (morning) flank of the northern (southern) polar cap.

Type F: Strong E_X along flanks of polar cap with weak fields in the central polar cap.

Type I: Irregular fields across the polar cap.

Types A and D (B) were found when the IMF was in a toward (away) structure.

During the last three months of 1976 the S3-2 orbit was close to the dawn-dusk meridian. Figure 8-17 is a scatter plot of Heppner's patterns observed in S3-2 data as a function of IMF B_X and B_Y. It is seen that A and B types are found only when $B_Y > 0$. For both OGO 6 and S3-2, A types are only found in the summer hemisphere and are associated with the IMF polarity that tends to produce strong E fields along the evening flank of the polar cap. The occurrence ration of A to B was 2:1 in S3-2 data; the A to D ratio was 3:1 in June 1969 OGO 6 data. The dependence of D types on B_Y (upper right plot) agrees with OGO 6. The type F patterns were found when $B_Y \sim 0$. The distribution of B, D, and F patterns tend to confirm the critical role of B_Y [Friis-Christensen et al., 1972]. A survey of S3-2 measurements shows that A, B, D, and F types are found when $B_Z < 0.5$ nT. Type I shows no correlation with B_X or B_Y. The highly irregular electric fields are found only when $B_Z > 0$. Type I patterns are further discussed below in connection with polar cap arcs.

An example of an E-field pattern that was found in approximately half the summer polar cap passes of S3-2 when $B_Z > 0.7$ nT is shown in Figure 8-18. During S3-2, Rev 5215 southern high-latitude pass B_Z was 4.9 nT [Burke et al., 1979]. As expected for driving sunward convection in the auroral oval, E_X was directed from dusk to dawn. At the poleward boundary of the oval, E_X reversed polarity becoming dawn to dusk near the morning and evening flanks of the polar cap. Within the central polar cap E_X was directed from dusk to dawn. Sunward convection in the central polar cap is inconsistent with a viscous interaction model. It was theoretically anticipated as a consequence of the magnetic merging model

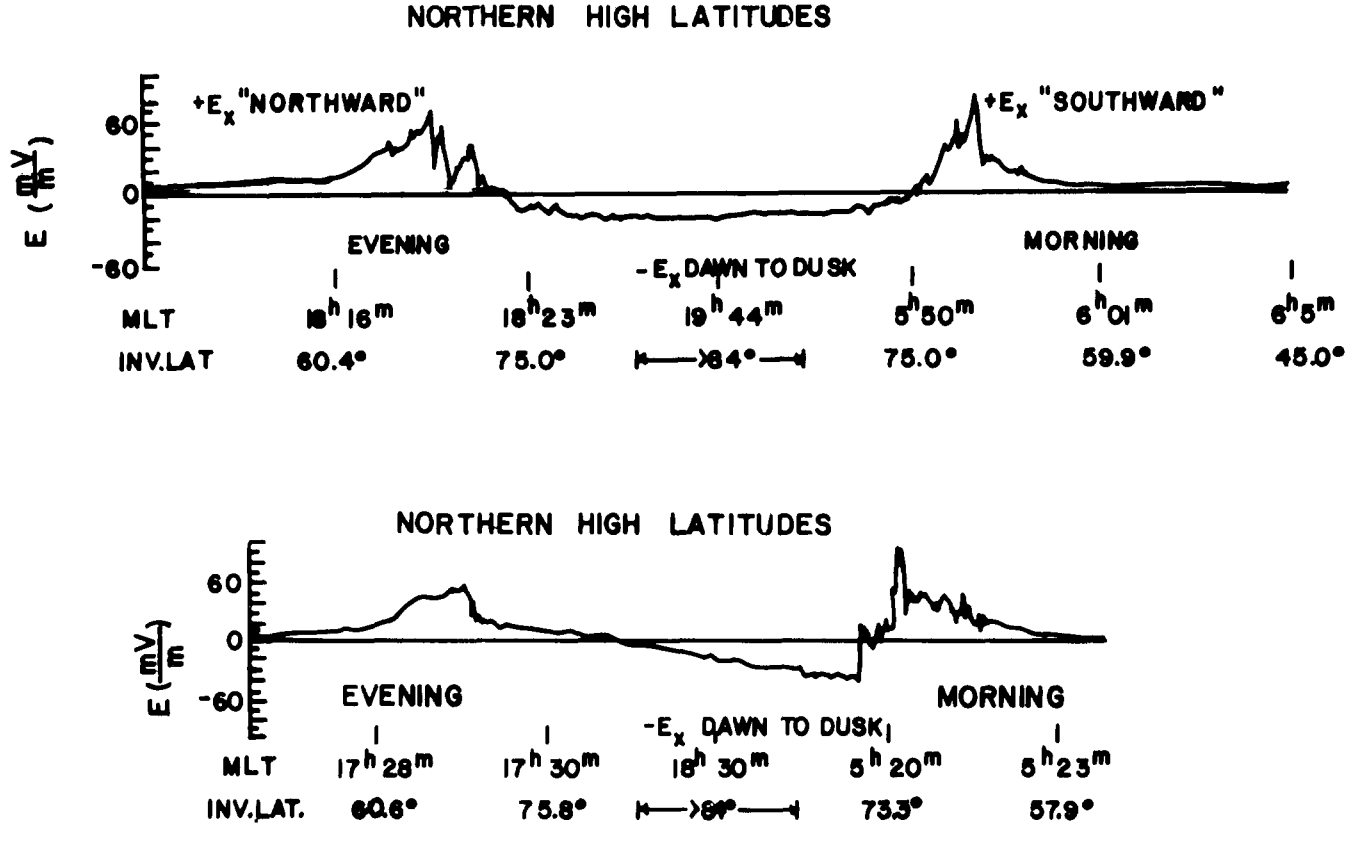

Figure 8-15. Two examples of large scale electric fields measured by OGO 6 [Heppner, 1972].

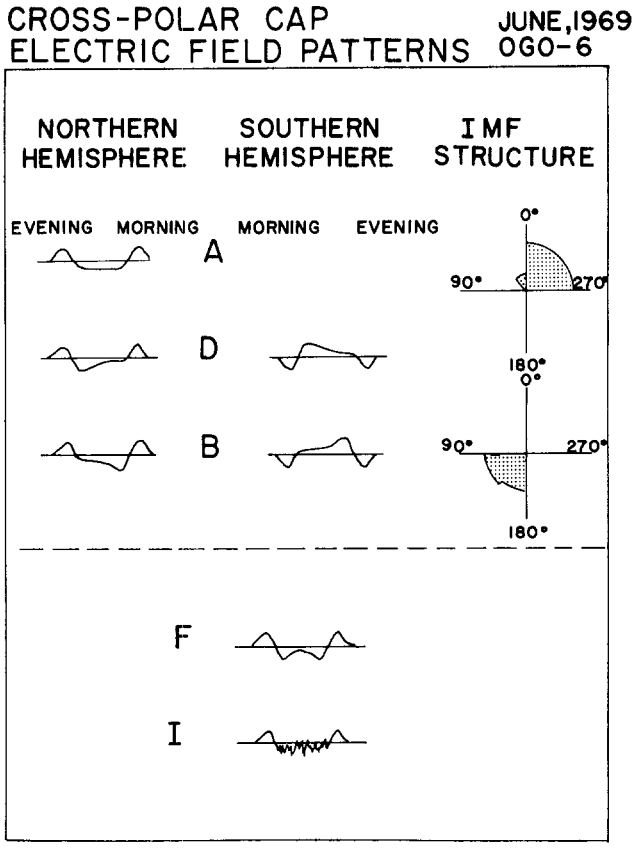

Figure 8-16. Types of electric field patterns observed by OGO 6 and their dependence of IMF B_X and B_Y [Heppner, 1972].

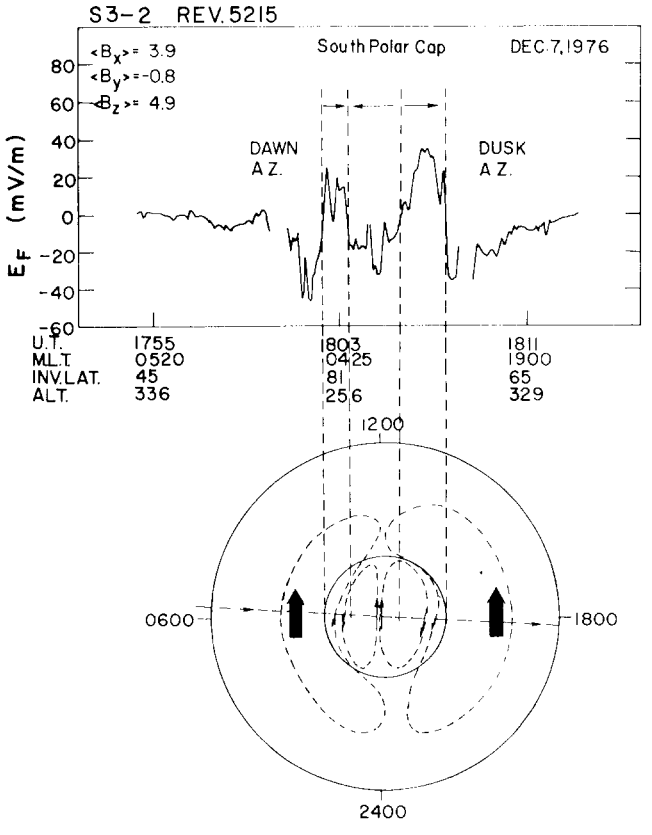

Figure 8-18. Example of sunward convection, dusk to dawn electric field in the central polar cap during a period of northern IMF.

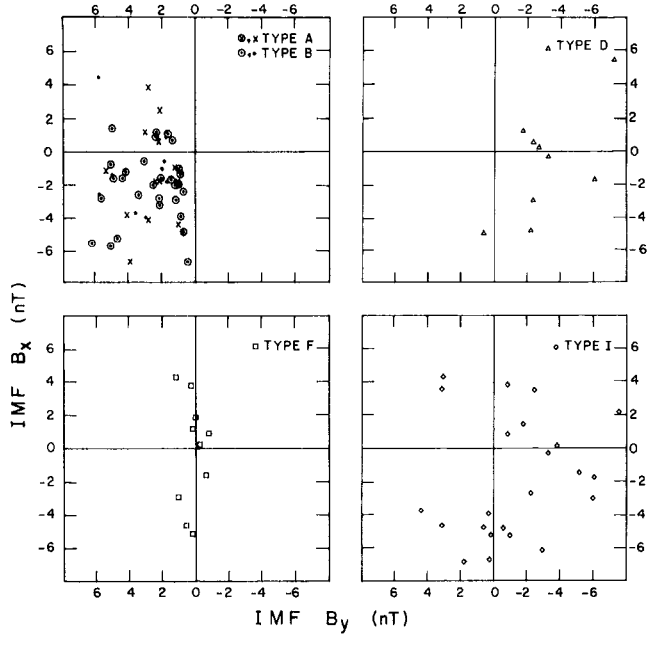

Figure 8-17. Scatter plot of convective electric field patterns observed by S3-2 as a function of IMF B_X and B_Y.

[Russell, 1972]. Sunward convection in the summer polar cap during periods of northward B_Z is consistent with both ground magnetometer [Maezawa, 1976] and laboratory simulation [Podgorny et al., 1978] results.

The cross polar cap potential $\Delta\Psi_{pc}$ can be derived from satellite electric field measurements and is an important parameter for magnetospheric modeling. This potential (in volts) gives the rate (in webers/s) that magnetic flux is transferred from the day to the night side of the magnetosphere. Based on two weeks of OGO 6 data Heppner [1977] found that on the average $\Delta\Psi_{pc}$ increased from 20 to 100 kV as the magnetic index Kp increased from 0 to 6. There were individual cases in which $\Delta\Psi_{pc}$ significantly exceeded 100 kV.

Reiff et al. [1981] analyzed 32 measurements of $\Delta\Psi_{pc}$ from AE-C and AE-D as a function of various solar wind and IMF parameters. To calculate merging rates that account for compression of the IMF in the magnetosheath, B at the magnetopause was set at the lesser of 8 times its solar wind value or 60 nT. The latter value was taken as typical of the earth's field near the subsolar magnetopause. Although the best agreement was found with theoretical merging rates, a high correlation was found with Akasofu's [1978] ε parameter. Figure 8-19 shows that in the AE measurements $\nabla\Psi_{pc}$

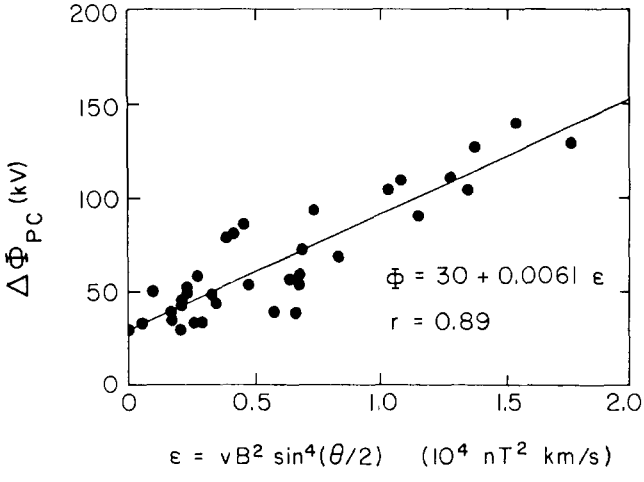

Figure 8-19. Cross polar cap potential as a function of solar wind parameter E [Heppner, 1977].

varied from 30 to 150 kV. This implies that 30 kV cannot be accounted for by merging. Such a potential greatly exceeds the potential across the boundary layer theoretically estimated by Hill [1979] and measured at ionospheric altitudes by Smiddy et al. [1980]. The upper limit of ~150 kV is much less than the cross magnetosphere potential drop ($\Delta\Psi_{sw}$) in the solar wind. With V_s = 400 km/s and B_Z = −5nT, the Y component of the electric field in the solar wind is 2 mV/m (= 12.8 kV/R_E). For a magnetospheric diameter of 30 R_E at the dawn-dusk meridian, $\Delta\Psi_{sw}$ = 384kV.

8.5.2 Polar Cap Precipitation

Particle fluxes into the polar ionosphere are conveniently divided into high and low energy components. Energetic particles from solar flares can seriously disrupt the polar ionosphere; these are important during magnetic storm periods. The flux levels of low energy protons in the polar cap are below the sensitivity levels of existing detectors. Winningham and Heikkila [1974] identified three classes of low energy electron precipitation: polar rain, polar showers, and polar squalls.

Polar rain is a relatively uniform type of precipitation that can fill the entire polar cap. Particles have mean thermal energies of ~100 eV and are isotropically distributed outside the atmospheric loss cone. The energy fluxes carried by these particles are in the 10^{-2} to 10^{-3} ergs cm^{-2} s^{-1} range, two to three orders of magnitude less than typical auroral fluxes. The highest energy fluxes for polar rain occur during periods of geomagnetic activity [Meng and Kroel, 1977]. Figure 8-20 is a plot of precipitating electron spectra measured in the dayside cusp and in the polar rain. The similarity in spectral shape suggests that polar rain particles are of direct magnetosheath origin. Particle fluxes measured in the

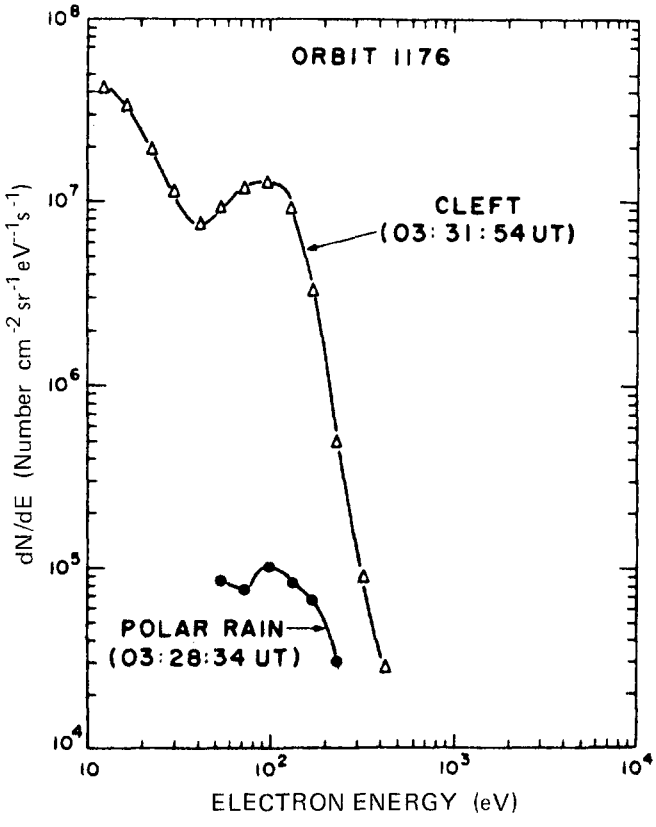

Figure 8-20. Typical differential spectra for the polar rain and cleft precipitation observed on orbit 1176 on 15 May 1969 [Winningham and Heikkila, 1974].

lobes of the magnetotail indicate that polar rain electrons enter the magnetosphere at great distance downstream from the earth. The efficiency of the entry process is modulated by the polarity of the IMF. Yaeger and Frank [1976] found that fluxes of soft electrons in the northern lobe of the tail increased by more than an order of magnitude when the IMF was in an away ($B_X < 0$) sector. There is also evidence suggesting a B_Y influence. Meng et al. [1977] found that the intensity of polar rain fluxes is strongest near the flank of the polar cap along which convection is strongest.

Polar showers are characterized by locally enhanced fluxes of precipitating electrons with mean energies of ~1 keV. These electron structures are embedded in broader regions of polar rain. They are thought to be responsible for sun-aligned arcs in the polar cap and are discussed further in Section 8.5.3.

Polar squalls are described by Winningham and Heikkila [1974] as localized, intense fluxes of electrons that have undergone field-aligned accelerations of several kV. They are found in the polar cap during geomagnetic storms. Foster and Burrows [1976; 1977] have reported observing fluxes of electrons into the polar cap that are spectrally identical to those found in polar squalls. However, these fluxes were observed to be widely and uniformly distributed over the polar cap. Like squall particles, they were observed during the recovery phases of magnetic storms. These fluxes also

appear to be modulated by the polarity of the IMF. While intense fluxes of keV electrons were measured in the northern polar cap, only polar rain was detected in the southern hemisphere. Figure 8-21 is a plot of particle fluxes measured

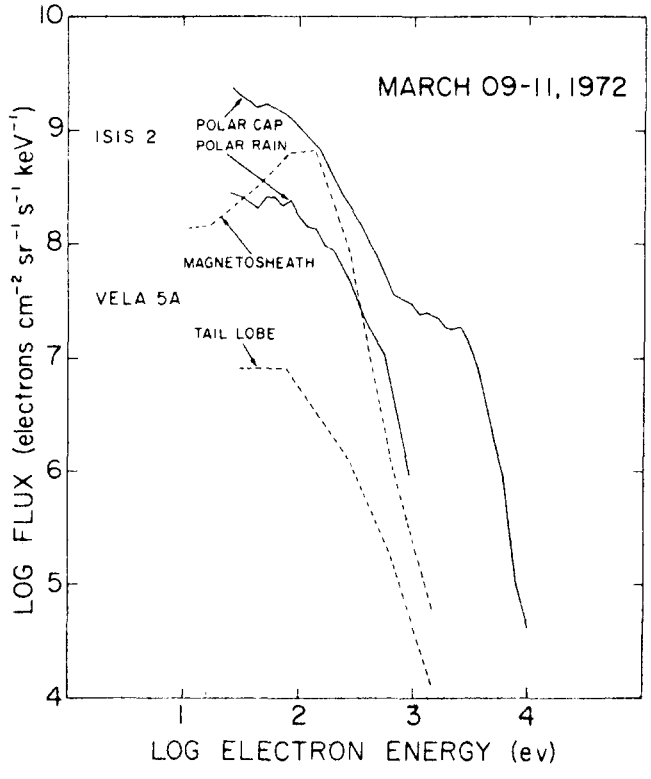

Figure 8-21. Differential electron energy spectra measured in the polar cap (solid curves) and in the tail lobe and magnetosheath (dashed curves). The magnetosheath measurement was made at ~13 hs on 9 March, the tail lobe at ~9 hs on 11 March, the polar cap at ~16 hours on 10 March, and the polar rain at ~11 hs 9 March. The polar cap spectra display a more or less pronounced high-energy tail relative to the magnetosheath [Foster and Burrows, 1976].

in the polar rain and extended squalls by ISIS 2 and nearly simultaneous measurements of electron fluxes in the magnetosheath and the tail lobe from VELA 5. Foster and Burrows [1977] argue from the near isotropy of the keV particles in the polar cap and the simultaneous absence of keV electrons in the magnetosheath that the electrons were accelerated along magnetic field lines at great distance from the earth in the magnetosphere.

8.5.3 Polar Cap Arcs

Investigations of discrete arcs in the polar cap have shown that polar cap arcs tend to be sun-aligned and are most frequently observed during periods of magnetic quieting when the IMF has a northward component [Ismail et al., 1977]. Visible arcs are caused by precipitating electrons with energies of $\leq$2 keV. Another class of subvisual arcs are produced at F-layer altitudes by electrons with energies of a few hundred eV [Weber and Buchau, 1977]. Here we illustrate many of the known characteristics of polar cap arcs using data from the USAF satellites S3-2 and DMSP (Defense Meteorological Satellite Program). At the times of interest, both satellites were in orbits close to the dawn-dusk meridian. S3-2 measured E_X, ΔB_Y (described in Section 8.5.1), and fluxes of electrons with energies between 50 eV and 17 keV. DMSP satellites are three-axis stabilized and are in circular, sun-synchronous orbit at an altitude of 840 km. All DMSP satellites are equipped with scanning, optical imagers [Eather, 1979]. Some, but not all, are also equipped with spectrometers that look toward local zenith and measure fluxes of electrons with energies between 50 eV and 20 keV.

Figure 8-22 is a cartoon that represents, in magnetic

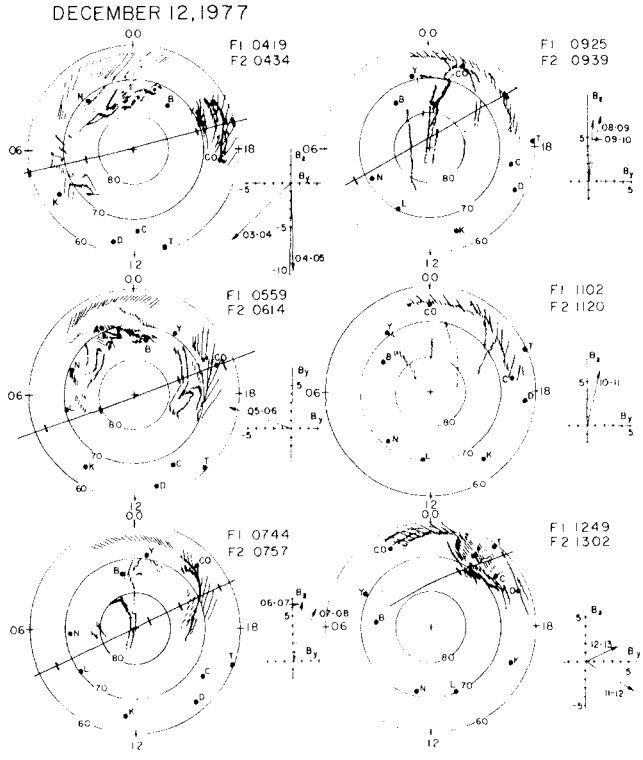

Figure 8-22. Cartoon representation of sequential DMSP high latitude imagery on 12 December 1977.

latitude and local time, composites of visible imagery from DMSP/F1 and DMSP/F2 taken over the northern hemisphere during a period of magnetic quieting on 12 December 1977. Straight solid lines give the portions of F2 trajectories during which electron data were taken. To the right of each cartoon, the hourly average values of IMF B_Y and B_Z are represented. During the initial period of southward B_Z, the polar cap was clear of visible emissions and only uniform, polar rain fluxes were detected. Approximately one hour after the IMF turned northward sun-aligned arcs were found in the polar cap. Polar cap arcs persisted until the IMF again turned southward. An hour after a second northward turning

of B_Z, arcs returned to the polar cap [Hardy et al., 1981]. The sun-aligned arcs were embedded in a region of high density (~0.1 cm^{-3}) polar rain. Within the arc the up-looking DMSP spectrometer detected three spectral components, a cold (100 eV) high density (1.5 cm^{-3}) population, a peaked primary distribution with a temperature of 350 eV that had been accelerated through a potential drop of ~750 volts and a secondary and/or degraded primary population. Burch et al. [1979] found that over polar showers the low-energy component was highly field-aligned. The secondary and accelerated primary populations were nearly isotropic in pitch angle.

Figure 8-23 gives a plot of E_X, ΔB_Y, the directional flux of electrons (cm^2 s sr)$^{-1}$ and electron pitch angles measured during S3-2 Rev 5231 as functions of invariant latitude, magnetic local time, and altitude. The pass occurred while the satellite was near apogee over the north polar cap where it passed within 1° of the magnetic pole along the dawn-dusk meridian. The IMF X, Y, and Z components were −3.7, 3.8 and 7.4 nT, respectively. As compared with the idealized measurements of Figure 8-14b, E_X and ΔB_Y were highly irregular. Recall that in the northern hemisphere E_X positive corresponds to sunward convection; $j_\parallel$ is out of the ionosphere in regions where ΔB_Y has a negative slope. Eight regions of negative slope in ΔB_Y accompanied by enhanced electron fluxes are noted in Figure 8-23. As evidenced by their being embedded in polar rain, Events 3 through 7 lie in the polar cap.

Event 6 has been analyzed in detail by Burke et al. [1982]. It was shown that the FAC out of the ionosphere had an intensity of 2.8 μ A/m^2 that was carried by electrons with a temperature of 200 eV and had been accelerated through a potential drop of ~1 kV. A nearly isotropic pitch angle distribution of electrons across event 6 suggests a field-

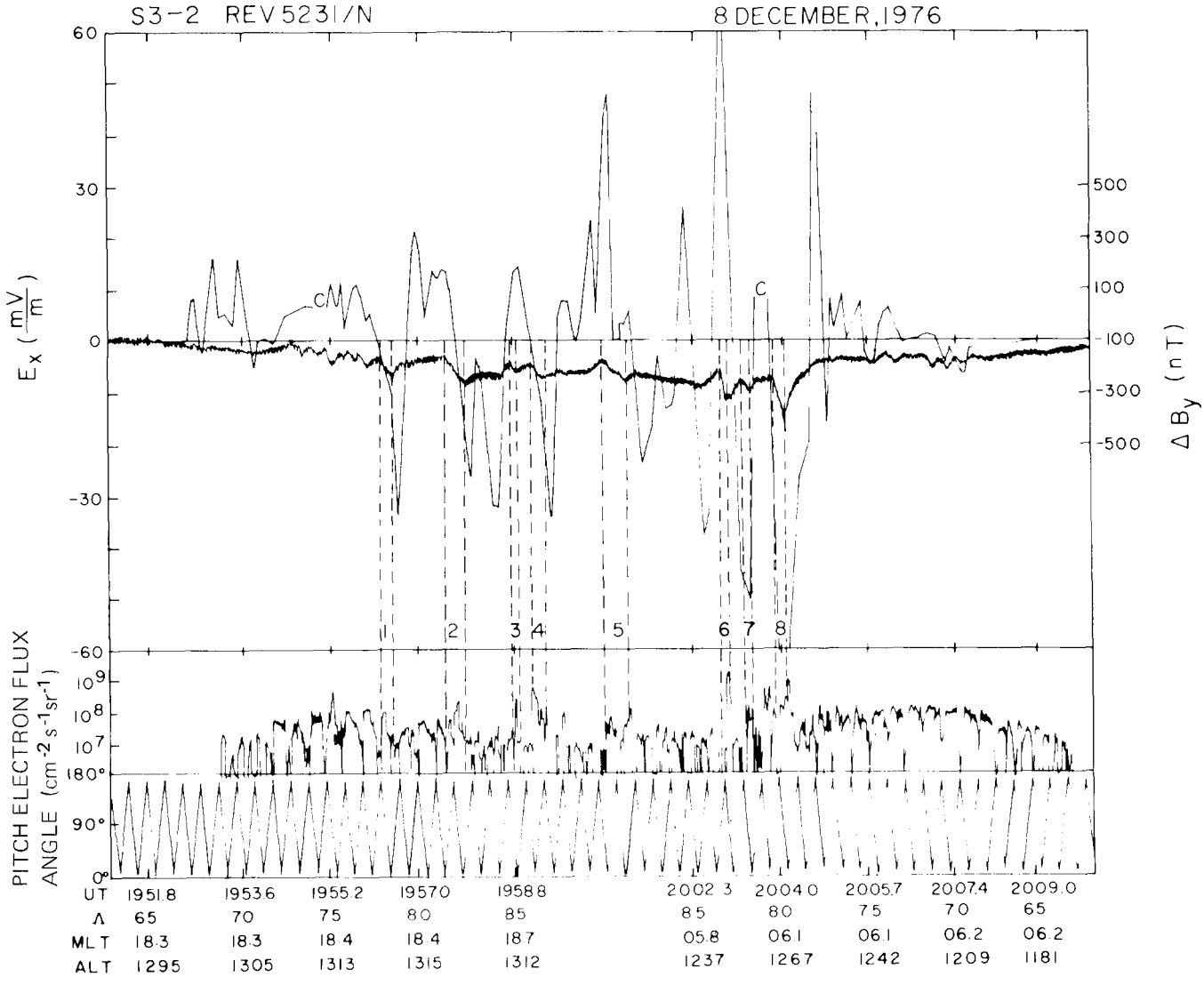

Figure 8-23. The top panel gives the dawn to dusk electric field component and the transverse magnetic field deflection (heavy line). The bottom panels give the directional electron flux and pitch angles. Data were taken over winter polar cap with IMF B_Z northward.

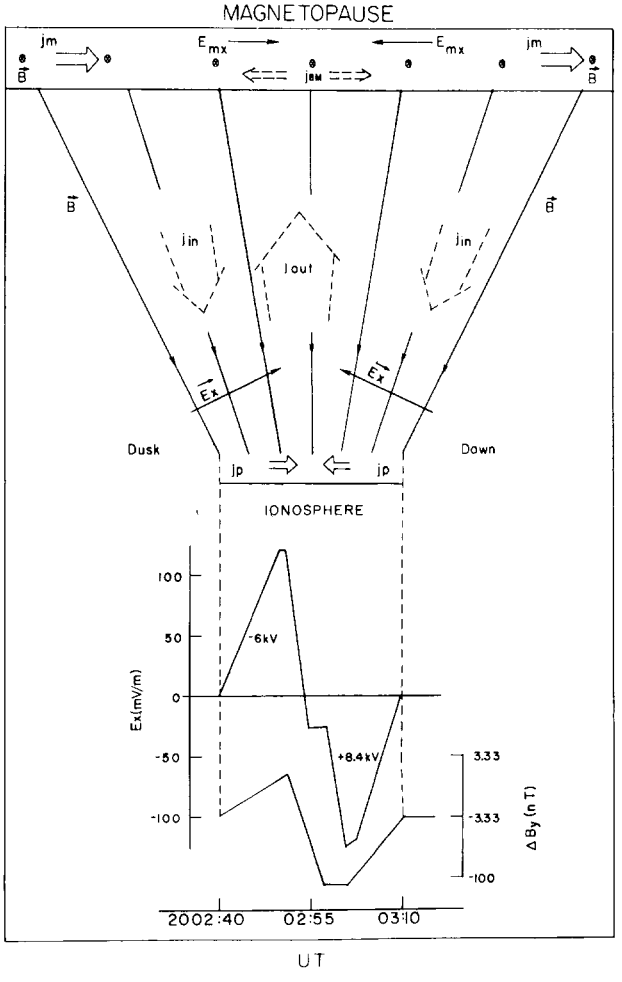

Figure 8-24. Idealized two dimensional projection of electric fields and currents in vicinity of Event 6 in Figure 8-23.

aligned potential drop extending for large distances along **B**. The measured electron energy fluxes of 2.5 ± 0.5 ergs cm^{-2} s^{-1} sr^{-1} were sufficient to produce a visible arc. Figure 8-24 gives an idealized, two-dimensional projection of the electric fields and currents associated with Event 6. As predicted by Lyons [1980;1981], the arc is in a region of negative electric field divergence. Similar, recently reported measurements from the Dynamics Explorer satellites suggest that such polar cap arcs may result from a bifurcation of the distant plasma sheet. That is, some polar cap arcs are on closed magnetic field lines [Frank et al., 1982].

8.6 AURORAL OVAL ELECTRODYNAMICS

The auroral oval is a region of closed magnetic field lines mapping through the plasma sheet. Ionospheric plasma convection should be mostly in the sunward direction. Near local midnight (noon) strong equatorward (poleward) convection components are expected.

The stock-in-trade vocabulary of a contemporary auroral physicist is replete with terms such as "inverted-Vs", "double-layers", "diffuse aurora", and "beams and conics" [Mozer et al., 1980]. These terms describe distinct auroral processes first reported in the 1970s. These new phenomena defy adequate summation in this section. Here we consider three main topics: (1) global auroral morphology, (2) phenomena associated with inverted-V events, and (3) substorms. Under the heading of global morphology we treat the systematics of large-scale, field-aligned current systems and the equatorward boundary of diffuse auroral precipitation.

8.6.1 Global Field Aligned Currents

The average global field-aligned current (FAC) system for periods of high and low magnetic activity are shown in Figure 8-14. Iijima and Potemra [1978] define Region 1 (2) as a region of FAC near the poleward (equatorward) portion of the auroral oval. In the evening sector current flows into the ionosphere in Region 2 and out in Region 1. The polarity of current flow is reversed in the morning sector. The intensities of these currents are of the order 1 $\mu A/m^2$. Currents out of the ionosphere are mostly carried by precipitating electrons. It is believed that cold electrons moving from the ionosphere to the magnetosphere carry the current into the ionosphere. Klumpar [1979] found that the equatorward boundary of Region 2 is coterminus with diffuse auroral electron precipitation in the post-midnight sector. In the evening sector, Region 2 extends ~2° equatorward of the electron precipitation boundary.

Near local midnight and noon large-scale FACs are the most complex. Figure 8-25 shows that near midnight the

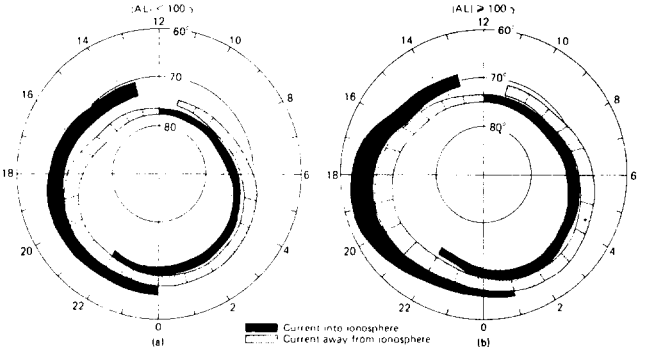

Figure 8-25. A summary of the distribution and flow directions of large-scale field-aligned currents determined from (a) data obtained from 439 passes of Triad during weakly disturbed conditions and (b) data obtained from 366 Triad passes during active periods [Iijima and Potemra, 1978].

morning side Region 1 current overlaps the evening side Region 1. No simultaneous electric field and magnetic field measurements have yet been reported from this region. However, it is expected that the morphology of these FACs can be understood in terms of latitudinal variations of the electric field just prior to local midnight. Maynard [1974]

showed that in the late evening sector the large scale convective electric field is directed poleward in the equatorward part of the oval. It rotates through west across the Harang discontinuity to equatorward in the poleward part of the oval. Pedersen currents driven in the ionosphere converge from both sides on the Harang discontinuity. To maintain an overall divergence-free current system, current must flow into the ionosphere at both the equatorward and poleward boundaries of the oval and out of the ionosphere near the Harang discontinuity. These are the essential features found near midnight in Figure 8-25.

In the vicinity of the dayside cusp an extra FAC system has been observed poleward of the Region 1. Its polarity is opposite to that of the nearby Region 1 current. In the northern (southern) hemisphere it appears only on the afternoon (morning) side of noon when IMF $B_Y < 0$, and only on the morning (afternoon) side when IMF $B_Y > 0$ [McDiarmid et al., 1979]. Simultaneous electric and magnetic field measurements from the USAF satellite S3-2 in the region of the dayside cusp suggest that the extra FAC system lies entirely on open, newly merged magnetic field lines that are being dragged toward the dusk or dawn flank of the polar cap [Doyle et al., 1981].

8.6.2 Equatorward Boundary of the Oval

In the previous section it was pointed out that the inner edge of the plasma sheet, or zero-energy Alfvén boundary, maps to the equatorward boundary of diffuse auroral precipitation. More than four thousand crossings of this boundary have been analyzed using data from an upward-looking electron spectrometer on the polar orbiting USAF satellites DMSP/F2 and DMSP/F4 [Gussenhoven et al., 1981]. The corrected geomagnetic latitudes of the boundaries (Λ_{CGM}) were studied as functions of magnetic local time (MLT) and Kp. Kp is a three-hour index of magnetic activity compiled from a world-wide network of midlatitude magnetometer stations. Results of linear correlation analyses

$$\Lambda_{CGM} = \Lambda_o + \alpha\, Kp$$

from available MLT sectors along with correlation coefficients are given in Tables 8-2 and 8-3. Using the magnetic field model of Fairfield and Mead [1975] the auroral boundaries were projected to the magnetospheric equatorial plane. Figure 8-26 is a plot of projected boundary positions (open circles) in comparison with predictions of the Volland-Stern electric field model [Ejiri et al., 1978] (solid line) and the injection boundary of Mauk and McIlwain [1974] (dashed lines). Best fits are obtained for a shaping factor $\gamma = 2$. Note that the stagnation points are offset from the dusk meridian. The offset angle ϕ_o varies from 23° toward evening for Kp = 0 to 45° toward afternoon for Kp = 5. The potential distribution in the equatorial plane (Equation (8.24) of the previous chapter) takes the form

$$\Psi\,(L, \phi) = \Omega\, B_o R_E^2 \left[\frac{L^\gamma}{\gamma L_S^{\gamma+1}} \sin(\phi - \phi_o) - \frac{1}{L}\right]. \tag{8.38}$$

For $\gamma = 2$ the term $1/\gamma\,(L_S^{\gamma+1})$is empirically related to Kp

$$\frac{1}{\gamma L_S^{\gamma+1}} = (1.6 + 2.4\ Kp) \cdot 10^{-4}$$

with a correlation coefficient of 0.97. Thus,

$$\Psi\,(L, \phi) = \Omega B_o R_E^2 \left[(1.6 + 2.4\ Kp)\ 10^{-4} L^2 \sin(\phi - \phi_o) - \frac{1}{L}\right]. \tag{8.39}$$

A further analysis [Hardy et al., 1982] has been performed correlating the boundary data and hourly averaged solar wind and IMF measurements. The most significant results were obtained when Λ_{CGM} was correlated with the interplanetary electric field VB_Z for the hour preceeding the boundary measurement subject to the condition $B_Z \leq 1$ nT. Correlation parameters are summarized in Table 8-4. To compare the results of the two studies a correlation analysis was performed between Kp and VB_Z.

With $B_Z \leq 1$ nT

$$Kp = 2.09 - 0.91\ VB_Z \tag{8.40}$$

Table 8-2. Regression coefficients for auroral boundaries in the morning sector.

	North				South			
MLT	Λ_o	α	N	cc	Λ_o	α	N	cc
0400–0500	67.4	−1.35	171	−0.58				
0500–0600	67.8	−1.87	365	−0.75				
0600–0700	68.5	−1.96	403	−0.82	67.4	−1.67	376	−0.74
0700–0800	70.2	−2.15	367	−0.83	68.3	−1.97	411	−0.81
0800–0900					68.7	−1.88	302	−0.72
0900–1000					69.1	−1.64	217	−0.67

Table 8-3. Regression coefficients for auroral boundaries in the evening sector.

	North				South			
MLT	Λ_o	α	N	cc	Λ_o	α	N	cc
1600–1700					71.3	−1.19	107	−0.65
1700–1800					70.7	−1.20	256	−0.69
1800–1900	71.6	−2.00	103	−0.90	70.6	−1.60	327	−0.80
1900–2000	71.2	−1.96	426	−0.89	70.0	−1.82	447	−0.87
2000–2100	69.4	−1.85	452	−0.82	69.5	−1.89	345	−0.84
2100–2200	68.7	−1.66	556	−0.83				
2200–2300	68.3	−1.79	184	−0.63				

with VB_z in mV/m. This allows us to express the magnetospheric potential as a function of VB_Z.

$$\Psi(L, \phi) = \Omega B_o R_E^2 \left[(6.6 + 2.2\ VB_Z)\ 10^{-4} L^2 \sin(\phi - \phi_o) - \frac{1}{L}\right]. \quad (8.41)$$

To test the validity of this equation it is possible to calculate the cross-magnetospheric potential drop ($\Delta\Psi_m$) and compare it with measured cross polar cap potential drops ($\Delta\psi_{pc}$).

To estimate $\Delta\Psi_m$ we use the position and shape of the magnetopause in the equatorial plane given by McIlwain [1972]. In this representation the magnetopause lies at a distance of $11R_E$ near the subsolar point and flares to a distance of $15R_E$ at the dawn-dusk meridian. We ignore stormtime compressions of the magnetosphere in the calculations. Two methods of calculating $\Delta\Psi_m$ are used. The first method sets $\phi_o = 0$ in Equation (8.40) making the axis of symmetry the

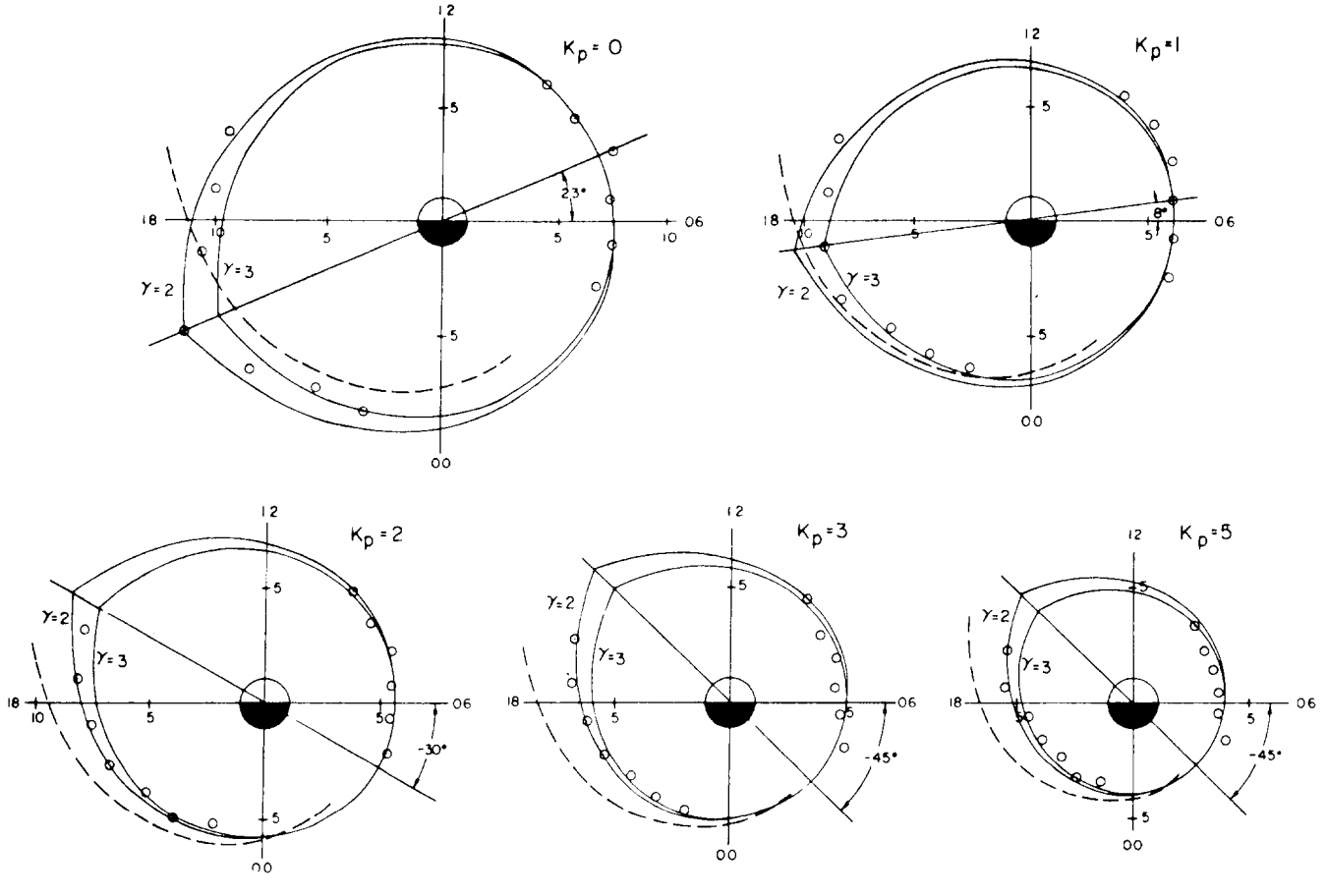

Figure 8-26. Volland-Stern injection boundaries for $\gamma = 2$ and $\gamma = 3$, rotated to fit the inner edge of the plasma sheet as determined by the DMSP/F2 auroral boundaries, for various Kp. The Mauk-McIlwain [1974] injection boundary is also shown (dashed line).

Table 8-4. The intercepts (Λ_o), slopes, correlation coefficients (cc) and sample sizes (N) for the linear regression of the boundary location with VB_Z in each magnetic local time zone, with a 1 h delay in the value of the interplanetary magnetic field (IMF) used.

	North Pole				South Pole			
MLT	Λ_o	Slope	cc	N	Λ_o	Slope	cc	N
0400–0500	65.1	3.28	0.52	43				
0500–0600	63.6	1.94	0.61	110				
0600–0700	64.2	1.80	0.70	105	64.4	1.70	0.56	124
0700–0800	66.1	2.56	0.68	85	63.7	1.95	0.61	94
0800–0900					65.1	2.27	0.69	68
0900–1000					65.5	1.74	0.74	38
1000–1100					65.8	0.44	0.59	19
1600–1700					69.5	1.89	0.82	26
1700–1800					68.6	1.36	0.74	57
1800–1900	68.6	2.49	0.81	44	67.2	1.60	0.70	83
1900–2000	67.3	1.76	0.68	123	66.6	1.81	0.70	141
2000–2100	65.2	1.71	0.70	130	65.8	2.01	0.64	44
2100–2200	65.5	1.91	0.71	132				

dawn-dusk meridian. The second method uses empirical values of ϕ_o given in Figure 8-26. For Kp = 0 the axis is tilted with the dusk stagnation point 23° to the nightward side of the dawn-dusk meridian. For higher values of Kp the stagnation point rotates sunward reaching a constant value of −45° for Kp > 2. In Figure 8-27 we have sketched the

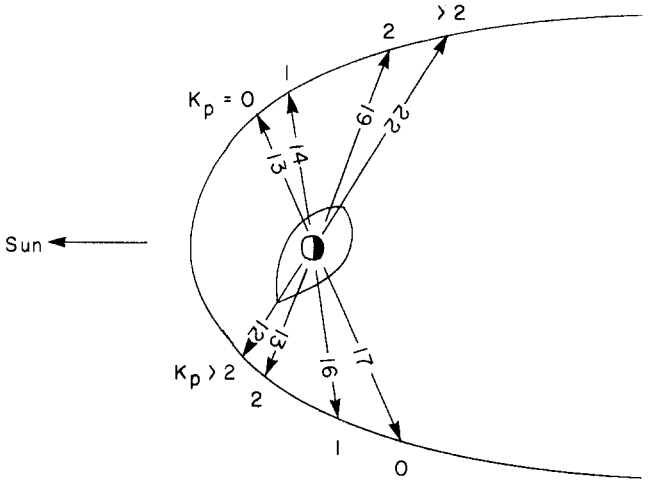

Figure 8-27. Equatorial magnetopause with distances along axes of symmetry for various values of Kp.

axes of symmetry indicating approximate distances to the dawn and dusk sides of the magnetopause for Kp = 0, 1, 2 and >2.

In Figure 8-28 $\Delta\Psi_m$ is plotted as a function of Kp, VB_Z and B_Z. VB_Z is positive when the interplanetary electric field (IEF) is directed from dawn to dusk (positive Y in standard geocentric, solar-magnetospheric coordinates). Values of B_Z are derived from VB_Z using a solar wind speed of 400 km/s. The solid line calculations assume $\phi_o = 0$, that is, the dawn-dusk meridian is the axis of symmetry. For this case, $\Delta\Psi_m$ increases linearly from 6.5 kV for Kp = 0 to 65 kV for Kp = 6. The dot-dash line indicates values of $\Delta\Psi_m$ using empirical values of ϕ_o and axes of symmetry indicated in Figure 8-27. In these calculations $\Delta\Psi_m$ ranges from 5.5 kV for Kp = 0 to 95 kV for Kp = 6. We note that in these calculations there is an abrupt transition in the trend of $\Delta\Psi_m$ near Kp = 2. This is close to our independently derived "breakpoint" in B_Z.

For reference, in Figure 8-28 we have also plotted average values of $B\Psi_{pc}$ (dashed line) as a function of Kp based on two weeks of OGO 6 electric field measurements. Heppner [1977] found that $\Delta\Psi_{pc}$ increased linearly from 20 kV for

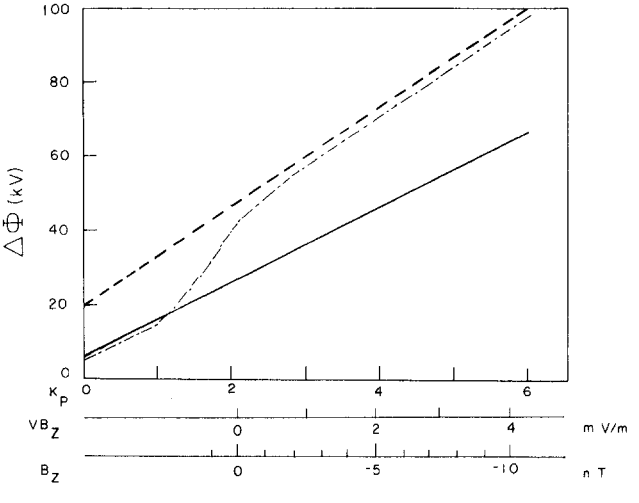

Figure 8-28. Polar cap potential, from Heppner [1977] (dashed line), and from Equation (8.12) with $\phi_o = 0$ (solid line) and ϕ_o with empirical values (dot-dash line).

Kp = 0 to 100 kV at Kp = 6. At low values of Kp the DMSP values of $\Delta\Psi_m$ are not sensitive to the value of ϕ_o and are considerably less than Heppner's $\Delta\Psi_{pc}$. With values of $\phi_o = -45°$ for Kp > 2 $\nabla\Psi_m$ and $\Delta\Psi_{pc}$ are of comparable magnitudes. In a time-average sense $\Delta\Psi_{pc}$ and $\nabla\Psi_m$ are coupled through the process of magnetic reconnection in the magnetotail. The two quantities must be roughly the same since on average, the amount of magnetic flux transferred to the nightside magnetosphere must equal the amount being returned to the dayside magnetosphere.

We emphasize that these are "average" results in the sense that they represent least square fits to the data. Heppner [1977] pointed out the $\Delta\Psi_{pc}$ frequently exceeds 100 kV during period of high Kp. Similarly, in both DMSP boundaries for cases of large negative B_Z and high Kp respectively, the latitude of the boundary is often much lower than the average. Since such cases correspond to the Alfvén boundary being closer than average to the earth, they also correspond to potentials exceeding 100 kV.

8.6.3 Inverted-V Phenomenology

Diffuse auroral electron precipitation is fairly uniform and isotropically distributed. In the poleward portion of the oval, electron fluxes are more spatially structured and are often field aligned. Discrete optical arcs are the most striking manifestation of the structuring process. The dominant structural features of electron fluxes observed with polar orbiting satellites are the so-called inverted-V structures. These structures are latitudinally narrow (~ 1°) bands of electron precipitation that increase in average energy from a few hundred eV to several keV, then return to a few hundred eV [Frank and Ackerson, 1971]. On energy-time spectragrams they have the shapes of inverted-Vs. Although individual inverted-V structures have been identified with ground-observed discrete arcs [Ackerson and Frank, 1972], the general relationship between the two phenomena is not clear. Inverted-Vs have latitudinal dimensions of several hundred km, whereas optical arcs have typical widths of 1 to 10 km [Maggs and Davis, 1968].

Lin and Hoffman [1979] have studied the global distribution of inverted-V structures and the pitch angle distribution of electrons within them. Figure 8-29 is an event occurrence map of 280 inverted-V structures observed with the AE-D satellite. This map shows that inverted-Vs are found throughout the high-latitude region. They appear predominantly in the late evening sector and are absent from the late pre-noon MLT sector.

The pitch angle distribution of electrons measured over an inverted-V event is given in Figure 8-30. This spectrogram gives the ratio of field-aligned flux at a given energy to the flux at pitch angles of 60°. The heavy black line gives the energy at which the maximum differential flux was measured. Note that the energy of the peak flux rises to ~3 keV at 1008:05 UT, then decreases to ~0.5 keV 20 seconds later. At the energy of the peak flux the electrons are field aligned whereas those with higher energies are isotropic over the downcoming hemisphere. This distribution is consistent with the electrons having been accelerated through a field-aligned potential drop at an altitude above the point of observation [Evans, 1974]. Electrons with energies less than that of the peak show highly complex pitch angle distributions. Some of these electrons are secondaries and degraded primaries trapped between a magnetic mirror point and an electrostatic potential barrier. Some of the low-energy electrons are highly field-aligned suggesting that they are accelerated electrons of ionospheric origin. If so, the complexity of their distribution suggests that the field-aligned potential drop is varying temporally and/or spatially.

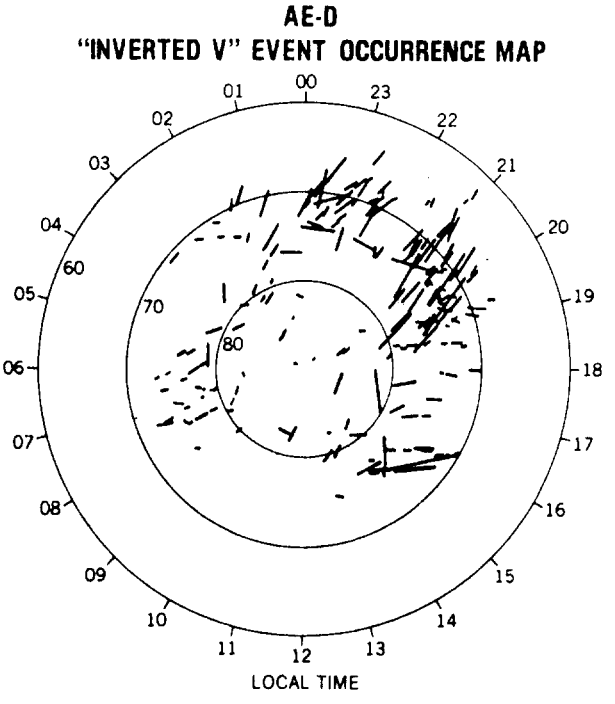

Figure 8-29. Spatial occurence map of 280 inverted-V events. Local time and circles of constant invariant latitude are shown as reference [Lin and Hoffman, 1979].

One of the most exciting developments of the 1970s was the development of direct evidence for the existence of field-aligned potential drops from measurements by instrumentation on the S3-3 satellite. The observational work of the University of California, Berkeley group is summarized by Mozer et al. [1980].

The highly eccentric orbit of S3-3 carried it to altitudes of ~8000 km above the auroral ionosphere. This is a hitherto unexplored region. At these altitudes very intense electric field structures were observed. An example given in Figure 8-31 shows electric fields at 8000 km reaching 400 mV/m and undergoing rapid reversals. If mapped, assuming $\mathbf{E} \cdot \mathbf{B} = 0$, to auroral arc altitudes the electric field intensities would be of the order of 1000 mV/m and the latitudinal width of the structure would be <10 km. This is a

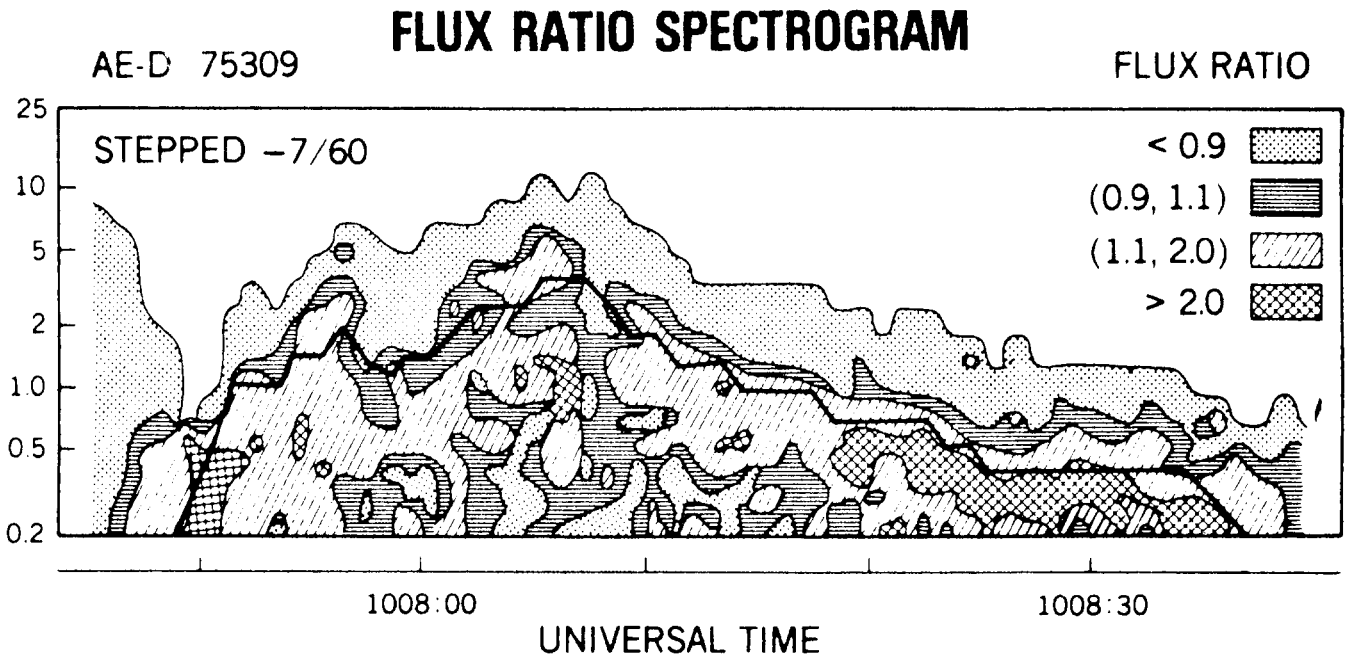

Figure 8-30. Spectrogram displaying the directional differential flux ratios (− 7°) and (60°) over an inverted-V event. The flux ratios are separated into four categories as shown in the upper right corner [Lin and Hoffman, 1979].

typical width of a discrete optical arc. However, the electric field intensity greatly exceeds that measured in the lower ionosphere. For this reason it is argued that there must be a potential drop along magnetic field lines that accelerate plasma sheet electrons to form arcs.

These electric field structures have been observed at all altitudes down to 1000 km. They are mostly found above 4000 km. Comparisons of S3-3 electric field measurements with simultaneous measurements from other instruments on the spacecraft show that the electric field structures are wave turbulence that are collocated with inverted-V precipitation structures. Within the electric field reversals we find fluxes of field-aligned electrons going into, and H^+ and O^+ ions going out of the ionosphere. The upgoing ions are decided according to pitch angle distributions into "beams" and "conics." Ion beams are highly directed along magnetic field lines. They have only been observed at altitudes greater than 4000 km and in the region of discrete rather than diffuse aurora. They are thought to be accelerated upward by the

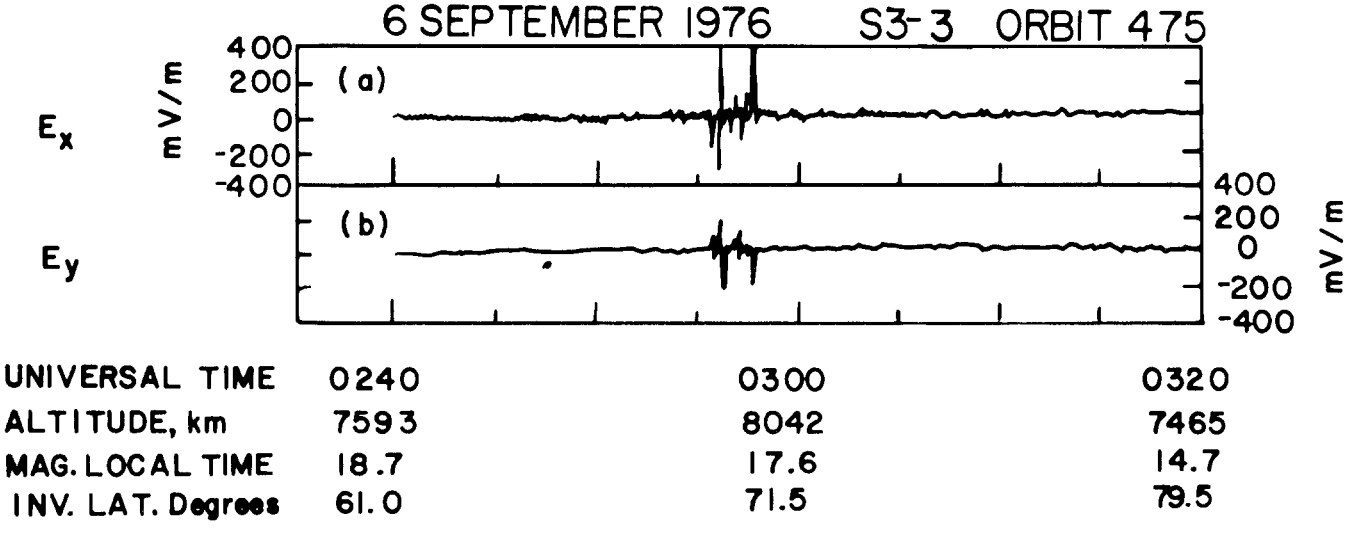

Figure 8-31. An example of a rapid electric field reversal observed at 8000 km by S3-3 [Mozer et al., 1980].

same parallel electric fields that accelerate plasma sheet electrons downward to form discrete auroral arcs. Ion conics have pitch angle distributions that peak at some intermediate angles between 90° and 0°. They have been detected at all latitudes in the auroral oval and at all altitudes greater than 1000 km. They are thought to be accelerated through resonant interactions with upper hybrid and ion cyclotron waves [Gorney et al., 1981].

8.6.4 Substorms

No overview of high-latitude electrodynamics would be complete without some comment, no matter how cursory, on substorms. It is during substorms that the dynamic coupling between the magnetosphere and ionosphere is most striking. Despite intensive studies of substorm processes over the last fifteen years, the richness of the observations has made total agreement on what constitutes the essential elements of a substorm elusive.

The evolution of discrete auroral arcs in the late evening sector as synopsized from all-sky camera data by Akasofu [1964] is given in Figure 8-32. Under pre-substorm conditions, homogeneous arcs extending for thousands of kilometers in the east-west direction are found in the oval and sun-aligned arcs are found in the polar cap. Substorm onset is announced by a brightening of the most equatorward arc. The discrete arcs expand poleward and westward traveling surges develops in the evening sector. After expanding to some maximum latitude, the arcs slowly retreat toward their pre-substorm condition.

To resolve differences between various schools of thought, nine active investigators met in August 1978 to specify substorm signatures and unambiguously define words commonly (often differently) used to describe substorm processes [Rostoker et al., 1980]. Major points of agreement were

1. During extended periods of northward IMF, the magnetosphere quiets and asymptotically approaches a ground state.
2. As the IMF turns southward, magnetospheric convection increases. This enhanced convection can exist for some time prior to substorm onset.
3. Substorm onset is signaled by an explosive increase in luminosity of the most equatorward arc, an intensification of the auroral electrojet, and a burst of Pi2 micropulsation. The burst of micropulsations testifies to the explosive nature of the onset process in the magnetospheric source region.
4. The expansion phase occurs from onset to the time when the midnight sector arcs have undergone their most poleward excursions. Note that in this definition, multiple intensifications of the substorm process, each marked by a micropulsation burst, are allowed.
5. The recovery phase coincides with the period in which midnight sector arcs retreat equatorward.

The substorm signatures dealt with in the August 1978 meeting are observable from ground-based instrumentation. Except for the micropulsation bursts, the signatures are of ionospheric effects whose causes lie in the magnetosphere. A key observation for understanding how substorms may be triggered comes from numerous satellites at geostationary altitude. During pre-substorm periods the nightside magnetic field at 6.7 R_E takes on a tail-like configuration. At substorm onset the magnetic field rapidly recovers its normal, nearly dipolar configuration. Simultaneously hot plasma sheet particles, with no dispersion, are injected.

To explain the observations the following scenario has been pieced together.

1. At a southward turning of the IMF, magnetic flux is transferred from the day to the night side of the magnetosphere. This process proceeds for about half an hour in which potential energy, in the form of stored magnetic flux, builds up in the tail. During this period the neutral sheet current moves earthward to $\sim$10 R_E leading to a tail like field geometry at 6.7 R_E. Recall that discrete arcs map to the boundary plasma sheet rather than the central plasma sheet. Thus, the most equatorward arc maps to a region near the inner edge of the neutral sheet current.
2. At substorm onset, the neutral sheet current near the inner edge of the boundary plasma sheet is diverted via field-aligned currents through the ionosphere. This leads to a collapse of the inner portion of the tail. In the ionosphere, part of the energy released in the collapse of the tail appears as an explosive brightening of the most equatorward arc. As the inner-tail field lines snap back to dipolar, plasma sheet electrons are rapidly accelerated by inductive electric fields and are injected to the vicinity of geostationary distance. The process continues while B_Z remains southward.
3. When the IMF turns northward the rate of flux transfer decreases abruptly. If the IMF maintains a northward component for considerable time, the potential energy stored in the tail is slowly dissipated and the magnetosphere relaxes toward a "ground state."

8.7 CONCLUSIONS

This chapter provides an introductory summary of what is known about the electrodynamics of the magnetosphere and the high latitude ionosphere prior to the launch of the Dynamics Explorer satellites. Our knowledge is an amalgam of theoretical models and *in situ* observations. In a qualitative sense, we are able to explain the gross features of magnetospheric processes. For example, a set of MHD equations has been used successfully to calculate the equilibrium shape of

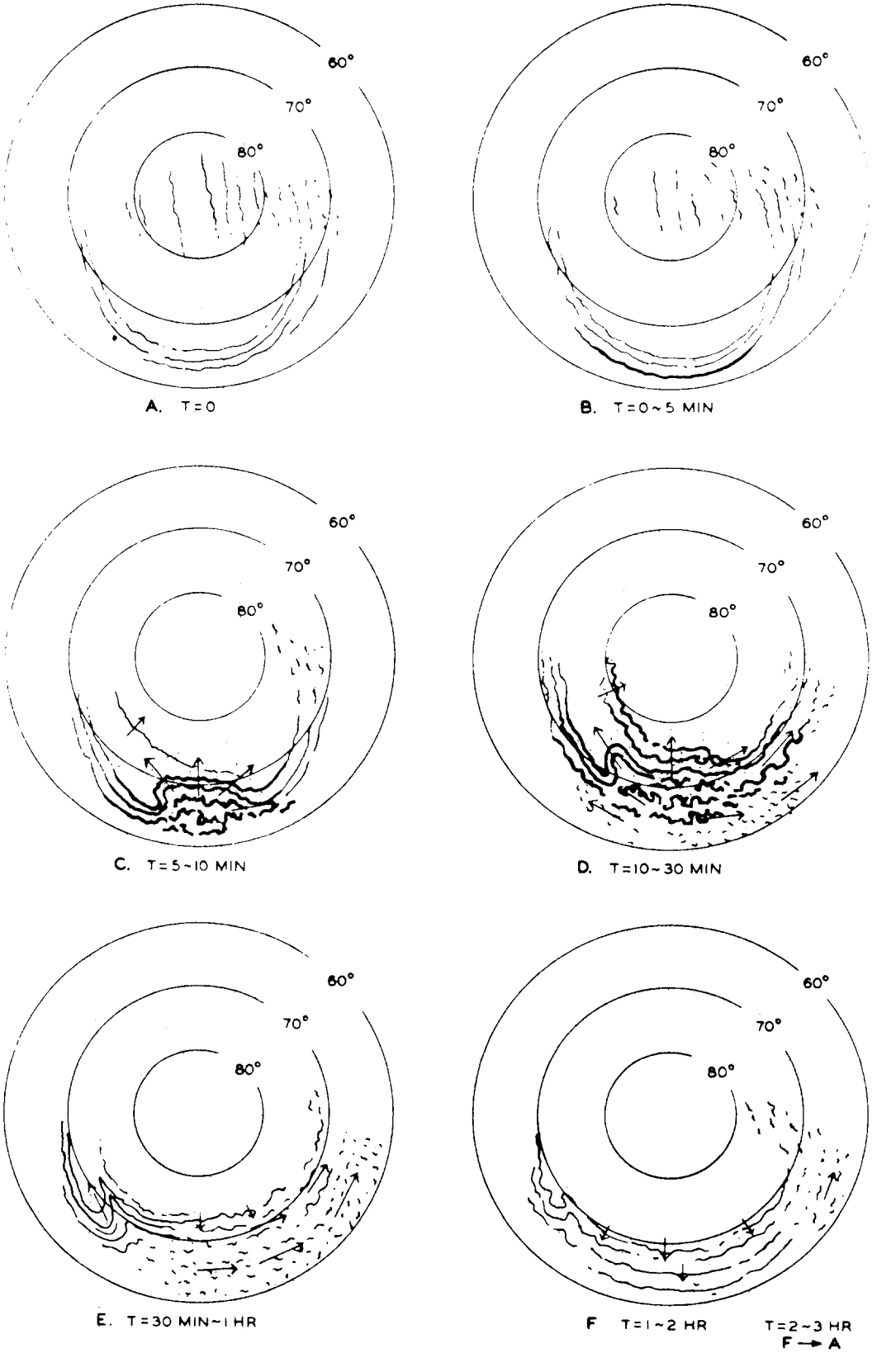

Figure 8-32. Schematic diagram to illustrate the development of the auroral substorm. The center of the concentric circles in each state is the north geomagnetic pole, and the sun is toward the top of the diagram [Akasofu, 1964]. (Reprinted with permission from Pergamon Press, Ltd. © 1964.)

the magnetopause [Mead and Beard, 1964]. However, the microphysics of how (if) magnetic merging occurs at the magnetopause and how particles cross the magnetopause to form the boundary layer are not yet understood. An essentially MHD model for coupling between the ionosphere and magnetosphere [Ashour-Abdalla and Thorne, 1978] has been applied to successfully simulate substorm effects in the inner plasma sheet and low latitude portion of the auroral oval [Lyons et al., 1979; Harel et al., 1981]. Thus, adiabatic energization is an important and well understood magnetospheric process. Other energization processes associated with reconnection in the magnetotail are not understood. The role of parallel electric fields for the formation of auroral arcs was experimentally established in the 1970s. Competing theoretical models of how parallel electric fields form in a collisionless plasma fill the literature.

With the gift of hindsight, it is interesting to examine the work of cartographers from the mid-seventeenth century. The mixed fruits of explorations spanning two hundred years are evident. Europe, the Middle East, Africa, and the eastern shores of the Americas are mapped with exquisite detail. Shapes assigned to the American west coasts and to the nations of East Asia range from vague to fanciful. Our own position twenty years into the age of satellite exploration is analogous to that of seventeenth-century map-makers. Some parts of the magnetosphere-ionosphere system are well explored. Our understanding of other important parts is based on fragmentary data samples and leaves much to be desired. Undoubtedly, readers a few decades hence will find many of our ideas as quaintly amusing as the seventeenth-century image of Japan. To those who view cartography or space physics as quasi-static processes, this is a scandalous situation. To those involved in the process, it crystalizes the excitement of exploration.

CHAPTER 8

REFERENCES

Ackerson K.L. and L.A. Frank, "Correlated Satellite Measurements of Low-Energy Electron Precipitation and Ground-Based Observations of a Visible Auroral Arc," *J. Geophys. Res.*, **77:** 1128, 1972.

Akasofu, S.-I., "The Development of the Auroral Substorm," *Planet Space Sci.*, **12:** 273, 1964.

Akasofu, S.-I., "Interplanetary Energy Flux Associated with Magnetospheric Substorms," *Planet Sp. Sci.*, **27:** 425, 1978.

Armstrong, J. and A.J. Zmuda, "Triaxial Magnetic Measurements of Field Aligned Currents at 800 km in the Auroral Region: Initial Results," *J. Geophys. Res.*, **78:** 6802, 1973.

Ashour-Abdalla M. and R.M. Thorne, "Toward a Unified View of Diffuse Auroral Precipitation," *J. Geophys. Res.*, **83:** 4755, 1978.

Axford W.I. and C.O. Hines, "A Unifying Theory of High-Latitude Geophysical Phenomena and Geomagnetic Storms," *Can. J. Phys.*, **39:**1433, 1961.

Burch, J.T., S.A. Fields and R.A. Heelis, "Polar Cap Electron Acceleration Regions," *J. Geophys. Res.*, **84:** 5863, 1979.

Burke, W.J., M.C. Kelley, R.C. Sagalyn, M. Smiddy, and S.T. Lai, "Polar Cap Electric Field Structure with a Northward Interplanetary Magnetic Field," *Geophys. Res. Lett.*, **6:** 21, 1979.

Burke, W.J., M.S. Gussenhoven, M.C. Kelley, D.A. Hardy, and F.J. Rich, "Electric and Magnetic Field Characteristics of Discrete Arcs in the Polar Cap," *J. Geophys. Res.*, **87:** 2431–2443, 1982.

Crooker, N.U., "Dayside Merging and Cusp Geometry," *J. Geophys. Res.*, **82:** 3629, 1977.

Crooker, N.U., "The Magnetospheric Boundary Layers: A Geometrically Explicit Model," *J. Geophys. Res.*, **84:** 951, 1979.

Doyle, M.A., F.J. Rich, W.J. Burke and M. Smiddy, "Field Aligned Currents and Electric Fields in the Region of the Dayside Cusp," *J. Geophys. Res.*, **86:** 5656, 1981.

Dungey, J.W. "Interplanetary Magnetic Field and the Auroral Zones," *Phys. Rev. Lett.*, **6:** 47, 1961.

Eastman T.E. and E.W. Hones Jr., "Characteristics of the Magnetospheric Boundary Layer and Magnetopause Layer as Observed by IMP 6," *J. Geophys. Res.*, **84:** 2019, 1979.

Eastman, T.E., E.W. Hones Jr., S.J. Bame, and J.R. Asbridge, "The Magnetospheric Boundary Layer: Site of Plasma Momentum and Energy Tranfer from the Magnetosheath into the Magnetosphere," *Geophys. Res. Lett.*, **3:** 685, 1976.

Eather, R.E., "DMSP Calibration," *J. Geophys. Res.*, **84:** 4134, 1979.

Ejiri, M., R.A. Hoffman, and P.H. Smith, "The Convection Electric Field Model for the Magnetosphere Based on Explorer 45 Observations," *J. Geophys Res.*, **83:** 4811, 1978.

Evans, D.S., "Precipitating Electron fluxes formed by a magnetic field-aligned potential difference," *J. Geophys. Res.*, **79:** 2853, 1974.

Fahleson, U.V., "Theory of Electric Field Measurements Conducted in the Magnetosphere with Electric Probes," *Space Sci Rev.*, **7:** 238, 1967.

Fairfield, D.H. and G.D. Mead, "Magnetospheric Mapping with a Quantitative Geomagnetic Field Model," *J. Geophys. Res.*, **80:** 535, 1975.

Foster, J.C. and J.R. Burrows, "Electron Fluxes Over the Polar Cap 1, Intense keV Fluxes During Poststorm Quieting," *J. Geophys. Res.*, **81:** 6016, 1976.

Foster, J.C. and J.R. Burrows, "Electron Fluxes Over the Polar Cap 2, Electron Trapping and Energization on Open Field Lines," *J. Geophys. Res.*, **82:** 5165, 1977.

Frank, L.A., "Initial Observations of Low-Energy Electrons in the Earth's Magnetosphere with OGO3," *J. Geophys. Res.*, **72:** 185, 1967.

Frank, L.A., "Relationship of the Plasma Sheet, Ring Current, Trapping Boundary, and Plasmapause Near the Magnetic Equator and Local Midnight," *J. Geophys. Res.*, **76:** 2265, 1971.

Frank L.A. and K.L. Ackerson, "Observations of Charged Particle Precipitation into the Auroral Zone," *J. Geophys. Res.*, **76:** 3612, 1971.

Frank, L.A., K.L. Ackerson and L.P. Lepping, "On Hot Tenuous Plasmas, Fireballs, and Boundary Layers in the Earth's Magnetotail," *J. Geophys. Res.*, **81:** 5859, 1976.

Frank, L.A., J.D. Cravens, J.L. Burch, and J.D. Winningham, "Polar View of Earth's Aurora with Dynamics Explorer," *Geophys. Res. Lett.*, **9:** 1001, 1982.

Freeman, J.W., "Internal Magnetospheric Plasma Flow," in *International Sydney Chapman Conference on Magnetospheric Boundary Layers, Alpbach, Austria, 1979* (ESA-SP-148), European Space Agency, Paris, 1979.

Friis-Christensen, E., K. Lassen, J. Willjelm, J.M. Wilcox, W. Gonzalez, and D.S. Colburn, "Critical Component of the Interplanetary Magnetic Field Responsible for Large Geomagnetic Events," *J. Geophys. Res.*, **77:** 3371, 1972.

Gold, T., "Motions in the Magnetosphere of the Earth," *J. Geophys. Res.* **64:** 1219, 1959.

Gorney, D.T., A. Clarke, D. Croley, J. Fennell, J. Luhmann, and T. Mizera, "The Distribution of Ion Beams and Conics Below 8000 km," *J. Geophys. Res.*, **86:** 83, 1981.

Gringanz, K.I., V.V. Bezrukikh, V.D. Ozerov and E.E. Rybchinskii, "A Study of the Interplanetary Ionized Gas, High Energy Electrons, and Corpuscular Radiation from the Sun by Means of the Three-Electrode Trap for Charged Particles on the Second Soviet Cosmic Rocket," *Sov. Phys. Dokl.* **5:** 361, 1961.

Gurnett, D.A. and L.A. Frank, "A Region of Intense Plasma Wave Turbulence on Auroral Field Lines," *J. Geophys. Res.*, **82:** 1031, 1977.

Gussenhoven, M.S., D.A. Hardy and W.J. Burke, "DMSP/F2 Electron Observations of Equatorward Auroral Boundaries and Their Relationship to Magnetospheric Electric Fields," *J. Geophys. Res.* **86:** 768, 1981.

Haerendel, G., G. Paschmann, N. Sckopke, H. Rosenbauer and P.C. Hedgecock, "The Frontside Boundary Layer of the Magnetosphere and the Problem Reconnection," *J. Geophys. Res.* **83:** 3195, 1978.

Hanson, W.B. and R.A. Heelis, "Techniques for Measuring Bulk Gas Motions from Satellites," *Space Sci Inst.*, **1:** 493, 1975.

Hardy, D.A., H.K. Hills, and J.W. Freeman, "A New Plasma Regime in the Distant Geomagnetic Tail," *Geophys. Res. Lett.* **2:** 169, 1975.

Hardy, D.A., M.S. Gussenhoven, E. Holman, W.J. Burke, and N. Heinemann, "DMSP/F2 Electron Observations of Equatorial Auroral Boundaries and Their Relationship to the Solar Wind Velocity and the North-South Component of the Interplanetary Magnetic Field," *J. Geophys. Res.*, **86:** 9961–9974, 1981.

Hardy, D.A., W.J. Burke, and M.S. Gussenhoven, "DMSP Optical and Electron Measurements in the Vicinity of Polar Cap Arcs," *J. Geophys. Res.*, **87:** 2413–2430, 1982.

Harel, M., R.A. Wolf, P.N. Reiff, R.W. Spiro, W.J. Burke, F.J. Rich, and M. Smiddy, "Quantitative Simulation of a Magnetospheric Substorm, 1, Model Logic and Overview, and 2, Comparison with Observations," *J. Geophys. Res.*, **86,** 2217, 1981.

Heppner, J.P., "Polar Cap Electric Field Distributions Related to the Interplanetary Magnetic Field Direction," *J. Geophys. Res.*, **77:** 4877, 1972.

Heppner, J.P., "Empirical Models of High-Latitude Electric Fields," *J. Geophys. Res.*, **82:** 1115, 1977.

Hill, T.W., "Generation of the Magnetospheric Electric Field," in *Quantitative Modelling of Magnetospheric Processes, AGU Monograph 21*, edited by W.P. Olson, American Geophysical Union, Washington D.C., p. 297, 1979.

Hines, C.O., "The Energization of Plasma in the Magnetosphere: Hydromagnetic and Particle Drift Approaches," *Planet. Space Sci.* **10:** 239, 1963.

Hones, Jr., E.W., J.R. Asbridge, S.J. Bame, M.D. Montgomery, and S. Singer, "Substorm variations of the magnetotail plasma sheet from $X_{SM} \approx -6\ R_E$ to $X_{SM} \approx -60\ R_E$," *J. Geophys Res.*, **78:** 1109, 1973.

Iijima, T. and T.A. Potemra, "Large-scale characteristics of field aligned currents associated with substorms," *J. Geophys. Res.*, **83:** 599, 1978.

Ismail, S., D.D. Wallis, and L.L. Cogger, "Characteristics of Polar Sun-Aligned Arcs," *J. Geophys. Res.*, **82:** 4741, 1977.

Johnson, F.S., "The Gross Character of the Geomagnetic Field in the Solar Wind," *J. Geophys. Res.*, **65:** 3049, 1960.

Kennel C. F. and H.E. Petschek, "Limit on Stably Trapped Particle Fluxes," *J. Geophys. Res.*, **71:** 1, 1966.

Kivelson, M.G., S.M. Kaye and D.J. Southwood, "The Physics of Plasma Injection Events," in *Dynamics of the Magnetosphere*, edited by S.-I. Akasofu, 385, D. Reidel, Dordrecht, Holland, 1979.

Klumpar, D.M., "Relationships Between Auroral Particle Distributions and Magnetic Field Perturbations Associated with Field Aligned Currents," *J. Geophys. Res.*, **84:** 6524, 1979.

Lemaire, J. and M. Roth, "Penetration of solar wind plasma elements into the magnetosphere," *J. Atmos. Ter. Phys.*, **40:** 331, 1978.

Lin, C.S. and R.A. Hoffman, "Characteristics of the Inverted-V Event," *J. Geophys. Res.*, **84:** 1514, 1979.

Lyons, L.R., "Generation of Large-Scale Regions of Auroral Currents, Electric Potentials, and Precipitation by the Divergence of the Convection Electric Field," *J. Geophys. Res.*, **85:** 17, 1980.

Lyons, L.R., "Discrete Aurora as the Direct Result of an Inferred High-Altitude Generating Potential Distribution," *J. Geophys. Res.*, **86:** 1, 1981,.

Lyons, L.R., D.S. Evans, and R. Lundin, "An Observed Relationship Between Magnetic Field Aligned Electric Fields and Downward Electron Energy Fluxes in the Vicinity of Auroral Forms," *J. Geophys. Res.*, **84:** 457, 1979.

Maezawa, K., "Magnetospheric Convection Induced by the Positive and Negative Z Components of the Interplanetary Magnetic Field: Quantitative Analysis Using Polar Cap Magnetic Records," *J. Geophys. Res.*, **81:** 2289, 1976.

Maggs, J.E. and T.N. Davis, "Measurement of the Thickness of Auroral Structures," *Planet. Space Sci.*, **16:** 205, 1968.

Mauk, B.H. and C.E. McIlwain, "Correlations of K_p with Substorm Injected Plasma Boundary," *J. Geophys. Res.*, **79:** 3193, 1974.

Maynard, N.C., "Electric Field Measurements Across the Harang Discontinuity," *J. Geophys. Res.*, **79:** 4620, 1974.

McDiarmid, J.B., J.R. Burrows, and M.D. Wilson, "Large Scale Magnetic Field Perturbations and Particle Measurements at 1400 km on the Dayside," *J. Geophys. Res.*, **84:** 1431, 1979.

McIlwain, C.E., "Plasma Convection in the Vicinity of Geosynchronous Orbit" in *Earth's Magnetospheric Processes*, edited by B.M. McCormac, 268, D. Reidel, Dordrecht, Holland, 1972.

Mead, G.D. and D.B. Beard, "Shape of the Geomagnetic Field Solar Wind Boundary," *J. Geophys. Res.*, **69:** 1169, 1964.

Meng, C.-I. and H.W. Kroel, "Intense Uniform Precipitation of Low-Energy Electrons Over the Polar Cap," *J. Geophys. Res.*, **83:** 2305, 1977.

Meng, C.-I., S.-I, Akasofu and K.A. Anderson, "Dawn-Dusk Gradient of the Precipitation of Low-Energy Electrons Over the Polar Cap and its Relation to the Interplanetary Magnetic Field," *J. Geophys. Res.*, **82:** 5271, 1977.

Mozer, F.S., R.B. Torbert, U.V. Fahleson, C.G. Falthammer, A. Gonfalone, A. Pedersen, and C.T. Russell, "Direct Observation of a Targential Electric Field Component at the Magnetopause," *Geophys. Res. Lett.*, **6:** 305, 1979.

Mozer, F.S., C.A. Cattell, M.K. Hudson, R.L. Lysak, M. Temerin, and R.B. Torbert, "Satellite Measurements and Theories of Low Altitude Auroral Particle Acceleration," *Space Sci. Rev.*, **27:** 155, 1980.

Northrop, T.G., *The Adiabatic Motion of Charged Paticles*, Chap. 3, Wiley, New York, 1963.

Olson, W.P., "The Shape of the Tilted Magnetopause," *J. Geophys. Res.*, **74:** 5642, 1969.

Pilipp, W.G. and G. Morfill, "The formation of the plasma sheet resulting from plasma mantle dynamics," *J. Geophys. Res.*, **83:** 5670, 1978.

Piddington, J.H., "Theories of the Geomagnetic Storm Main Phase," *Planet. Space Sci.*, **11:** 1277, 1963.

Podgorny, I.M., E.M. Dubinin, and Yu. N. Potanin, "The Magnetic Field on the Magnetospheric Boundary from Laboratory Simulation Data," *Geophys. Res. Lett.*, **4:** 207, 1978.

Reiff, P.H., R.W. Spiro, and T.W. Hill, "Dependence of Polar-Cap Potential Drop on Interplanetary Parameters," *J. Geophys. Res.*, **86:** 7639, 1981.

Rich, F.J., D.L. Reasoner, and W.J. Burke, "Plasma Sheet at Lunar Distance: Characteristics and Interactions with the Lunar Surface," *J. Geophys. Res.* **78:** 8097, 1973.

Rosenbauer, H., H. Grunwalt, M.D. Montgomery, G. Paschmann, and N. Sckopke, "HEOS 2 Plasma Observations in the Distant Polar Magnetosphere: The Plasma Mantle," *J. Geophys. Res.*, **80:** 2723, 1975.

Rossi, B. and S. Olbert, *Introduction to the Physics of Space*, Chapter 5, McGraw-Hill, New York, 1970.

Rostoker, G., "Magnetospheric and Ionospheric Currents in the Polar Cusp and Their Dependence on the B_y Component of the Interplanetary Magnetic Field," *J. Geophys. Res.*, **85:** 4167, 1980.

Rostoker, G., S.-I. Akasofu, J. Foster, R.A. Greenwald, Y. Kamide, K. Kawasaki, A.T.Y. Lui, R.L. McPherron, and C.T. Russell, "Magnetospheric Substorms—Definitions and Signatures," *J. Geophys. Res.*, **85:** 1663, 1980.

Russell, C.T., "The Configuration of the Magnetosphere," in *Critical Problems of Magnetospheric Physics*, edited by E.R. Dyer, 1, National Academy of Science, Washington, D.C., 1972.

Russell, C.T. and R.C. Elphic, "ISEE Observations of Flux Transfer Events at the Dayside Magnetopause," *Geophys. Res. Lett.*, **6:** 33, 1979.

Sckopke, N., G. Paschmann, H. Rosenbauer, and D.H. Fairfield, "Influence of the Interplanetary Magnetic Field Oneral and Thickness of the Plasma Mantle," *J. Geophys. Res.*, **81:** 2687, 1976.

Sckopke, N., G. Paschmann, G. Haerendel, B.U.O. Sonnerup, S.J. Bame, T.G. Forbes, E.W. Hones, Jr., and C.T. Russell, "Structure of the Low-Latitude Boundary Layer," *J. Geophys. Res.*, **86:** 2099, 1981.

Smiddy, M., et al., "Effects of High Latitude Conductivity on Observed Convection Electric Fields and Birkeland Currents," *J. Geophys. Res.*, **85:** 6811, 1980.

Southwood, D.J. and S.M. Kaye, "Drift Boundary Approximations in Simple Magnetospheric Convection Models," *J. Geophys. Res.*, **84:** 5773, 1979.

Speiser, T.W., "Particle Trajectories in Model Current Sheets, II: Application to Auroras Using a Geomagnetic Tail Model," *J. Geophys. Res.* **72:** 3919, 1967.

TerHaar, D., *Elements of Hamiltonian Mechanics*, Chapter 6, North Holland, Amsterdam, 1964.

Vasyliunas, V. M., "A Survey of Low-Energy Electrons in the Evening Sector of the Magnetosphere with OGO 1 and OGO 3," *J. Geophys. Res.*, **73:** 2839, 1968.

Vasyliunas, V.M., "Mathematical Models of Magnetospheric Convection and its Coupling to the Ionosphere," in *Particles and Fields in the Magnetosphere*, edited by B.M. McCormac, D. Reidel, Dordrecht, Holland, 1970.

Vasyliunas, V.M., *Magnetospheric Plasma, in Solar Terrestrial Physics*, edited by E. Dyer, D. Reidel, Dordrecht, Holland, p. 192, 1972.

Vasyliunas, V.M., "Interaction Between the Magnetospheric Boundary Layers and the Ionosphere," *International Sydney Chapman Conference on Magnetospheric Boundary Layers, Alpbach, Austria, 1979* (ESA-SP-148), European Space Agency, Paris, 1979.

Weber, E.J. and J. Buchau, "Polar Cap F-Layer Auroras," *Geophys. Res. Lett.*, **8:** 125, 1981.

Williams, D.J. and L.R. Lyons, "The Proton Ring Current and Its Interaction with the Plasmapause: Storm Recovery Phase," *J. Geophys. Res.*, **79:** 4195, 1974.

Winningham, J.D. and W.J. Heikkila, "Polar Cap Auroral Electron Fluxes Observed with Isis 1," *J. Geophys. Res.*, **79:** 949, 1974.

Yaeger, D.M. and L.A. Frank, "Low Energy Electron Intensities at Large Distances Over the Earth's Polar Cap," *J. Geophys. Res.*, **81:** 3966, 1976.

Young, T.S.T., J.D. Callen and J.E. McCune, "High Frequency Electrostatic Waves in the Magnetosphere," *J. Geophys. Res.*, **78:** 1082, 1973.